Porosity, Pore Structure, and Fluid Distribution in the Sediments Entering the Northern Hikurangi Margin, New Zealand

Jade Dutilleul, Sylvain Bourlange, Yves Géraud, Didier Stemmelen

JGR Solid Earth

RESEARCH ARTICLE
10.1029/2020JB020330

Porosity, Pore Structure, and Fluid Distribution in the Sediments Entering the Northern Hikurangi Margin, New Zealand

Jade Dutilleul[1], Sylvain Bourlange[1], Yves Géraud[1], and Didier Stemmelen[2]

[1]GeoRessources, Université de Lorraine, CNRS, Nancy, France, [2]LEMTA, Université de Lorraine, CNRS, Nancy, France

Key Points:
- The Northern Hikurangi margin input section is characterized by contrasted fluid distribution, pore structure, and potential for excess pore pressure buildup
- It is essential to use corrected porosity instead of apparent porosity in clay-rich sediments and altered oceanic crust
- The future décollement may develop in the lower part of pelagic carbonates or at the top of volcaniclastic facies of the Hikurangi Plateau

Supporting Information:
- Supporting Information S1

Correspondence to:
J. Dutilleul,
jade.dutilleul@univ-lorraine.fr

Citation:
Dutilleul, J., Bourlange, S., Géraud, Y., & Stemmelen, D. (2020). Porosity, pore structure, and fluid distribution in the sediments entering the northern Hikurangi margin, New Zealand. *Journal of Geophysical Research: Solid Earth*, *125*, e2020JB020330. https://doi.org/10.1029/2020JB020330

Received 3 JUN 2020
Accepted 10 OCT 2020
Accepted article online 14 OCT 2020

Abstract Hosting both tsunami earthquakes and slow slip events at shallow depth, the northern Hikurangi margin has motivated strong research efforts over the last two decades to better understand the relation between fluid pressure and fault mechanical behavior. Recently, IODP Expeditions 372 and 375 drilled, cored, and logged the basin entering this subduction zone providing a unique opportunity to characterize initial hydrogeological and petrophysical properties that drive seismic hazards along the margin. We inventory bound and interstitial fluid contents and assess the compaction state of the heterogeneous incoming sequence by correcting shipboard total connected porosity from the bound water content that typically characterizes clay-rich sediments. By combining mercury injection capillary pressure, nuclear magnetic resonance, and nitrogen gas adsorption, we further document the evolution of pore structure with increasing depth. We also compare porosity data at the logging and sample scales. Both logging and laboratory data evidence contrasted porosity, pore structure, and fluid distribution across the entering section. Shallow macroporous siliciclastic units show very low bound water content and undergo compaction-induced dewatering as they are normally consolidated during burial. In contrast, mesoporous volcaniclastic Hikurangi Plateau facies are characterized by high potential for bound water release from smectite, zeolite, and opal dehydration at greater depths. They mostly exhibit very low permeability except potentially in uncemented highly porous intervals where the décollement may initiate. Macroporous to mesoporous pelagic carbonates sandwiched in between exhibit mixed behavior and may also host the future décollement, similarly to the southern part of the margin.

1. Introduction

It has been evidenced that the interplay between fluid flow and tectonic processes critically affects fault mechanical behavior and thus controls seismic hazard (Moore & Vrolijk, 1992; Saffer & Tobin, 2011; Saffer & Wallace, 2015). At subduction zones, large volumes of fluids are produced by mechanical compaction and mineral dehydration reactions associated with the dewatering of incoming materials when they are accreted or subducted. At shallow depths, burial and possibly lateral tectonic loading results in the mechanical compaction of the pore network of input sediments with continuous production of interstitial water associated with a decrease in interstitial porosity and possibly permeability until lithification into rocks (e.g., Fagereng et al., 2018). In contrast, dehydration reactions affect both incoming sediments and igneous crust in specific pressure-temperature windows, resulting in a transient release of water bound to hydrous minerals (e.g., Fagereng et al., 2018; Kameda et al., 2012; Kastner et al., 2014; Pytte & Reynolds, 1989). Smectite transformation to non-expandable illite through intermediate mixed-layers interstratified is the largest low temperature (<150°C) dehydration-driven fluid source contributing to fluid production at shallow depths with compaction-induced dewatering (e.g., Bekins & Dreiss, 1992; Bray & Karig, 1985; Ellis et al., 2015; Hüpers et al., 2017; Hüpers & Kopf, 2012; Saffer, 2003). Zeolites, lawsonite, and chlorite dehydrations are higher-grade metamorphic reactions that occur deeper (Fagereng et al., 2018; Kastner et al., 2014). The produced fluids flow to the surface through stratigraphic or structural drains (Bourlange & Henry, 2007; Saffer & Tobin, 2011). Fluids may remain trapped in lower permeability sediments, possibly resulting in compartmentalized high fluid pressure approaching or exceeding lithostatic values (Moore & Vrolijk, 1992). Several studies have outlined that spatial variations of the input sedimentary column thickness and mineralogical composition (especially clay content), thermal state, hydration state of the igneous crust critically affect fluid production, flow, and trapping and thus the distribution of fluid pressure across subduction margins (e.g., Ellis et al., 2015; Hüpers et al., 2017; Kitajima & Saffer, 2014; Saffer & Tobin, 2011, and references

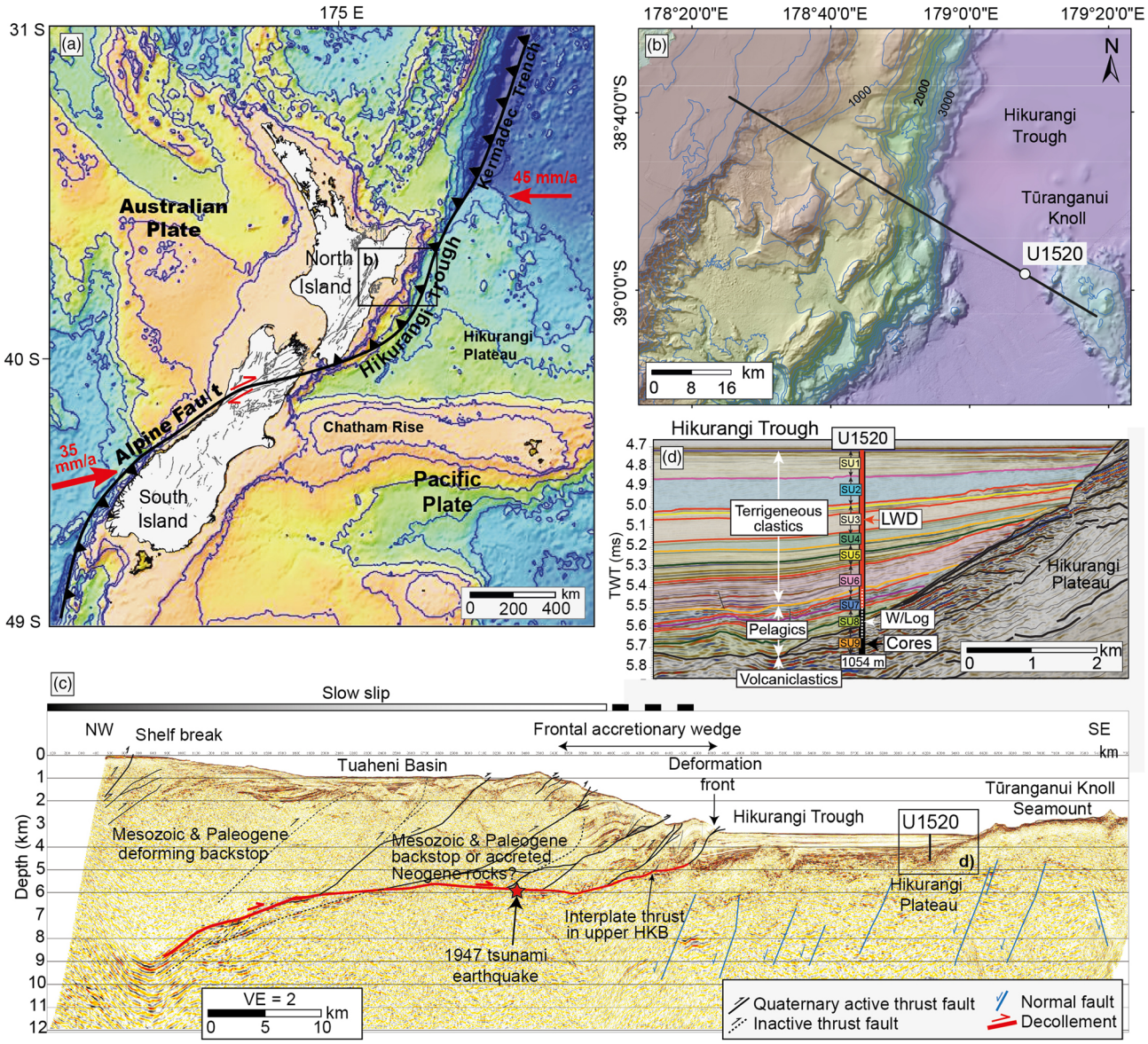

Figure 1. (a) Tectonic setting of the Hikurangi margin with plate motion indicated by red arrows. (b) Bathymetric map of the IODP Expeditions 372/375 study area offshore Gisborne located on (a). The black line represents (c) the seismic profile 05CM-04 across the margin with a (d) zoom in on Site U1520 showing seismic units (SU), main lithological packages and coring/logging intervals. The red star shows the projected location of March 1947 tsunami earthquake and VE means vertical exaggeration. (a), (b), (c), and (d) are modified from Wallace et al. (2019).

therein; Underwood, 2007). Fluid pressure is thought to modulate the location of the updip and downdip transitions of the seismogenic locked zone along the subduction plate interface and is associated with a wide range of slip modes (Saffer & Tobin, 2011, and references therein) with specific hazards for coastal populations and infrastructures. In particular, elevated fluid pressure has been proposed to facilitate tsunami earthquake propagation to the trench (e.g., Bilek & Lay, 2002; Dean et al., 2010; Geersen et al., 2013; Seno, 2002), slow slip events (e.g., Bassett et al., 2014; Bell et al., 2010; Kodaira et al., 2004; Liu & Rice, 2007; Saffer & Wallace, 2015) and tremors (e.g., Obara, 2002). The relations between slip modes and fluids are particularly well studied at the northern Hikurangi margin, offshore Gisborne, on the eastern part of North Island, New Zealand (Figure 1a) where the Pacific Plate subducts obliquely beneath the Australian Plate at ~4.5 cm/year (Wallace et al., 2004). There, the plate interface generates both tsunami earthquakes (Doser & Webb, 2003) and particularly shallow slow slip events that have been intensively studied since the installation of a dense continuous GPS network in the 2000s (Bartlow et al., 2014;

Beavan et al., 2007; Koulali et al., 2017; Wallace, 2020; Wallace & Beavan, 2010; Wallace et al., 2012, 2016, 2017). These slow slip events recur every 1 or 2 years with slow slip propagating close to the seafloor ≤2,000 mbsf and potentially all the way to the trench along the plate interface and/or splay faults within the prism (Fagereng et al., 2019; Shaddox & Schwartz, 2019; Wallace et al., 2016; Wallace & Beavan, 2010) and may be associated with tectonic tremors (Todd et al., 2018). Slow slip events are shallow sourced (≤15 km) in a zone where high-amplitude seismic reflectors locally occur, likely corresponding to fluid-rich subducted sediments (Bell et al., 2010; Ellis et al., 2015) or specific lithologic high-reflectivity packages like volcanic material (Saffer et al., 2019).

In order to characterize the lithological, mineralogical, physical, hydrogeological, thermal, and geochemical properties of input sediments and how these properties are affected by the subduction process giving rise to various slip styles in the shallow portion of the northern Hikurangi margin, International Ocean Discovery Program Expeditions 372 and 375 drilled, cored, and logged Site U1520 offshore Gisborne, ~95 km from the shore and ~16 km oceanward of the deformation front (Figures 1b and 1c). This site revealed an extremely heterogeneous input section composed by Paleocene to Quaternary siliciclastic and carbonate sedimentary rocks and the top of the Late Cretaceous oceanic crust of the Hikurangi Plateau (Figures 1d and 2c). Here, we characterize the initial fluid content and compaction state of this incoming sequence. Following previous works, we use post-cruise geochemical data like cation exchange capacity (CEC) to correct total connected porosity (equivalent to shipboard MAD porosity in Wallace et al., 2019) from elevated bound water content typical of clay-rich sediments to determine interstitial porosity that is representative of compaction state, unlike total connected porosity. We further characterize the evolution of macropore to micropore structure with increasing depth by combining mercury injection capillary pressure (MICP), nuclear magnetic resonance (NMR), and nitrogen gas adsorption (N_2GA). We interpret the evolution of porosity regarding variations of lithology, mineralogy, and deformation structures across the sedimentary section. Finally, we discuss these relationships in terms of potential for fluid production and fluid pressure generation by compaction-induced dewatering or mineral dehydration along the northern Hikurangi margin and any implications for the location of décollement initiation that is not well constrained yet (Barnes et al., 2020).

2. Samples, Data, and Method

2.1. Lithology and Sampling of the Input Sedimentary Sequence

At Site U1520, the Quaternary siliciclastic part of the input section (Figures 2b and 2c) corresponds to Unit I (~0–110 mbsf), Unit II (~110–222 mbsf), and Unit III (~222–510 mbsf). Unit I is trench-wedge facies with greenish gray silty clay to clayey silt hemipelagites with abundant thick turbiditic interbeds of silt and sand. Unit II is also silty clay to clayey silt hemipelagites with thin silty turbiditic interbeds only and corresponds to part of the distal edges of the Ruatoria debris avalanche. Unit III is trench-wedge facies with dark greenish gray silty clay to clayey silt hemipelagites with thin turbiditic interbeds of silt and beds of light gray volcanic ash. The subducting Hikurangi Plateau is locally protruded by seamounts (e.g., Turanganui Knoll) (Davy et al., 2008) resulting in a Unit I to Unit III sequence that is relatively condensed at Site U1520 and that thickens toward the deformation front (Wallace et al., 2019). Unit IV (~510–848 mbsf) is Paleocene to early Pleistocene pelagic carbonate facies composed mostly of light greenish gray marls from ~510 to 776 mbsf and chalks from ~776 to 848 mbsf. An interval of light brownish gray calcareous mudstone (~721–739 mbsf), matrix-supported carbonate conglomerates with volcaniclastic clasts interpreted as gravity flow deposits and thin layers of volcanic ash/tuff are also sandwiched in between marl and chalk deposits. Units V (~848–1,016 mbsf) and VI (~1,016–1,045 mbsf) are Late Cretaceous aged and mostly correspond to reddish brown, greenish, dark bluish, or grayish volcaniclastic conglomerates with granule-sized altered basaltic clasts, with intervals of grayish yellow to pinkish marls, dark gray clayey siltstones, and siliceous mudstones, above basalt. We picked up 106 core samples with one sample per core in average in Units I–IV (i.e., one sample every 10 m) and refined sampling in Units V and VI where dramatic change in volcaniclastic facies occur over length scales ranging a few to tens of centimeters (Barnes et al., 2020; Wallace et al., 2019). Samples were taken as close as possible from the samples that were squeezed for shipboard interstitial water composition analysis. Samples were shipped and stored at chilled temperature (2–8°C) in sealed plastic bags with a sponge saturated with seawater to preserve moisture. Post-cruise analyses on samples were compared to geophysical data that include logging-while-drilling data (0 to ~750 mbsf) and wireline logging data (~642–947 mbsf).

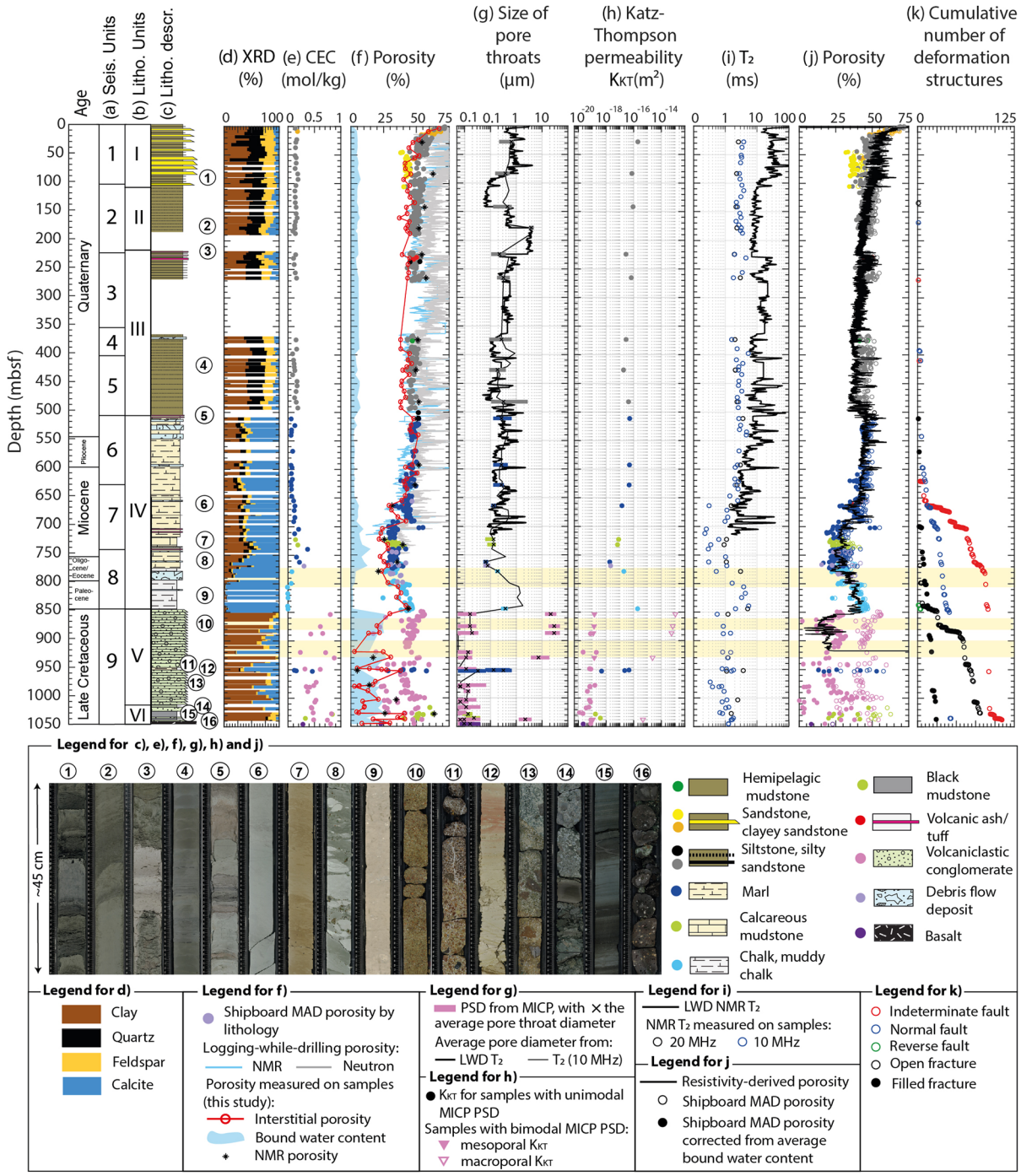

Figure 2. Synthesis of lithological, structural and petrophysical properties at Site U1520. Lithological data include (a) seismic units, (b) lithological units, and (c) lithological description modified after Wallace et al. (2019) with examples of cores (1 to 16), (d) mineralogy from shipboard XRD and (e) cation exchange capacity. Physical properties include porosity (f and j), (g) pore size distribution (PSD) from MICP (where bars represent pore throat diameters corresponding to at least 40% of the maximal mercury injection shown in Figure S4) and determined from NMR, (h) Katz-Thompson permeability and (i) NMR T_2 measured on discrete samples and by the LWD tool. Structural data include (k) deformation structures identified during Expeditions 372–375. Yellow shaded zones locate chloride anomalies. The color of the data points in (e), (f), (g), (h), and (j) indicates lithology: green for hemipelagic mudstones with convoluted mud clasts; light green for black siliceous mudstones or calcareous mudstones; gray for alternating silt(stone) and mud(stone); black for silt(stone); gold for alternating sand(stone) and mud(stone); yellow for sand(stone); red for volcanic ashes; navy blue for marls; light blue for chalks and muddy chalks; pink for volcaniclastic conglomerates; lavender for debris flow deposits and purple for basalt. (1) U1520D11H1A41-84 cm; (2) U1520D21F1A60-105 cm; (3) U1520D 27F1A15-60 cm; (4) U1520D42X2A30-75 cm; (5) U1520D51X1A25-70 cm; (6) U1520C4R3A15-60 cm; (7) U1520C11R3A20-65 cm; (8) U1520C15R2A3-48 cm; (9) U1520C21R1A60-104 cm; (10) U1520C26R3A27-71 cm; (11) U1520C34R1A40-85 cm; (12) U1520C34R4A2-46 cm; (13) U1520C37R3A55-99 cm; (14) U1520C41R1A32-76 cm; (15) U1520C42R3A25-70 cm; (16) U1520C44R1A80-123 cm.

2.2. Quantification of Porosity

2.2.1. Estimation of Bound Water Content and Interstitial Porosity From CEC, Soluble Chloride Content, and Interstitial Water Composition

In smectite-rich sediments, fluid content includes interstitial water in the macropore to micropore space and bound water that is located in the interlayer space and electrostatically bound on particle surfaces because of the compensation of negatively charged smectite layers by hydrated cations. The chemical composition of interstitial water is typically close to that of seawater (i.e., chloride-bearing) while bound water is chloride-free. Smectite hydration properties are mainly driven by the type of interlayer cation and the amount and location of layer charge (Ferrage et al., 2006; Ransom & Helgeson, 1995) that affects interlayer water content and thickness. Smectites can contain up to 25 wt% of interlayer water by incorporating up to three layers of water molecules in the expandable interlayer space. Interlayer water is typically organized in one, two, or three layers corresponding to 6–8, 12–16, and 18–24 water molecules per cation charge (Henry, 1997) and to a thickness of 11.8–12.9, 14.5–15.8, and ~18–19.1 Å, respectively. The interlayer space thickness can be characterized by XRD from the evolution of the d(001) basal-spacing or layer-to-layer distance (e.g., Ferrage, 2016; Ferrage et al., 2006). Bound water content can be calculated from CEC that is the number of sites on mineral surfaces that can exchange ions with interstitial water. Interstitial porosity can then be determined by correcting total connected porosity from bound water content (e.g., Brown & Ransom, 1996; Conin et al., 2011; Dutilleul et al., 2020; Henry, 1997; Henry & Bourlange, 2004).

Total connected porosity was measured according to Blum's (1997) procedure that is also followed shipboard (Wallace et al., 2019). The wet mass (m_{wet}) of the sample is weighted before drying the sample for 24 hr in a convection oven at 105°C ± 5°C to remove all the water present (i.e., interstitial and bound water) (Daigle, 2014; Ellis & Singer, 2007). The sample is then cooled to room temperature in a desiccator during 2 hr before measuring its dry mass (m_{dry}) and dry volume (V_{dry}) using a Micromeritics® AccuPyc II 1340 helium-displacement pycnometer. The calculation of total connected porosity ϕ_t and grain density ρ_g is corrected for the precipitation of salt during drying:

$$\phi_t = \frac{V_f}{V_{wet}} = \frac{V_f}{V_f + V_{dry} - V_{salt}}, \tag{1}$$

$$\text{and } \rho_g = \frac{m_s}{V_s}, \tag{2}$$

where $V_f = \frac{m_f}{\rho_f}$ is the volume of pore fluid with $m_f = \frac{m_w}{1-s}$ the pore fluid mass, $m_w = m_{wet} - m_{dry}$ is the pore water mass, s is the salinity (0.035), and ρ_f is the density of pore fluid (1.024 g/cm^3), $V_{salt} = \frac{m_{salt}}{\rho_{salt}} = \frac{m_w\, s}{(1-s)\ \rho_{salt}}$ is the salt volume with m_{salt} the salt mass and ρ_{salt} the density of salt (2.220 g/cm^3), $m_s = m_{wet} - m_f = m_{dry} - m_{salt}$ is the mass of solids excluding salt, and $V_s = V_{dry} - V_{salt}$ is the volume of solids excluding salt.

Dry samples were then ground for chemical analyses using a Retsch® mixer mill MM 200 with agate grinding beads and jars, except the samples from Units V and VI that were ground using an annular mill with tungsten jar and grinding tools. CEC was measured by exchange with cobaltihexamine and ultraviolet-visible spectrometer Varian SpectrAA 800 Zeeman. In this study, CEC is an average value over all the minerals of the sample and is thus a reliable indicator of the hydrous mineral composition of the samples. Exchangeable cation composition (Na^+, K^+, Ca^{2+}, and Mg^{2+}) was measured by atomic absorption spectrometer Thermo Scientific ICE 3300. Soluble chloride content per dry mass was determined by sequential water extraction (Tessier et al., 1979) and ion chromatography. Chemical analyses were carried on at the Laboratoire Interdisciplinaire des Environnements Continentaux (LIEC) in Nancy and Metz, France.

Interstitial porosity ϕ_i and bound water content ϕ_b are determined from the total connected porosity ϕ_t, the average number of water molecules per cation charge n, the water molar mass (M_w = 0.018 kg/mol), the density of pore fluid ρ_f, the grain density ρ_g, and the CEC:

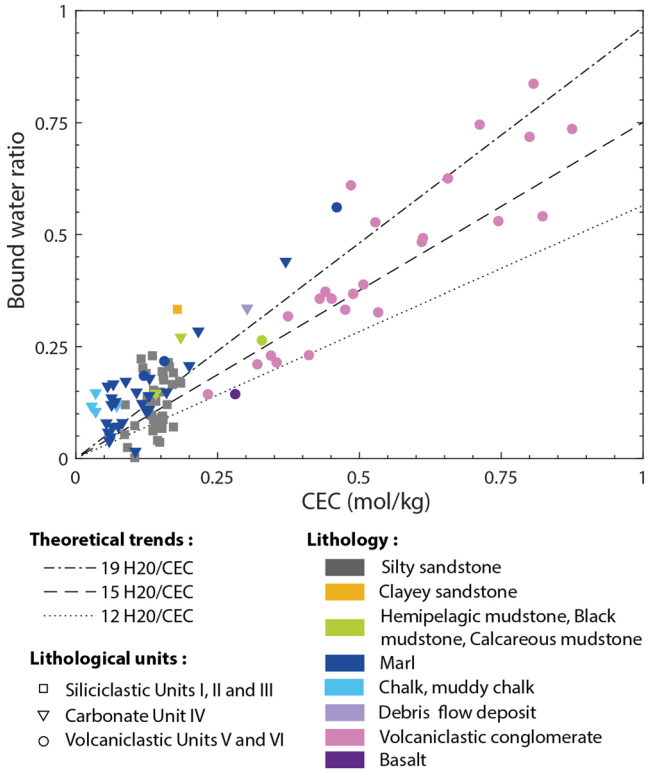

Figure 3. Volume of chloride-free fluid per volume of grain (bound water ratio) versus cation exchange capacity for 106 samples from Site U1520 per lithological units and detailed lithology. Theoretical trends n are from Henry and Bourlange (2004) and Conin et al. (2011) and correspond to ideal two (respectively three) water layers smectite containing 12 and 15 (respectively 19) water molecules per cation charge (Henry, 1997).

$$\phi_i = \phi_t - \phi_b = \phi_t - n\frac{M_w}{\rho_f} CEC\, \rho_g(1-\phi_t). \quad (3)$$

The average number of water molecules per cation charge n typically ranges from 12 to 15 (i.e., smectite with two layers of water) and is expressed

$$n = \frac{\rho_w W_b}{\rho_g CEC\, M_w}, \quad (4)$$

with ρ_w the density of bound water (chloride-free water, ρ_w = 1,000 kg/m^3), w_b the bound water ratio (Conin et al., 2011; Dutilleul et al., 2020; Henry, 1997; Henry & Bourlange, 2004), which is the volume of bound water ($V_{f(Cl\ free)}$) per volume of solid:

$$w_b = \frac{V_{f(Cl\ free)}}{V_s} = \frac{V_f}{V_s} - \frac{V_{f(Cl)}}{V_s}. \quad (5)$$

The volume of chloride-bearing water $V_{f(Cl)}$ was determined from the soluble chloride concentration per dry mass measured on samples and the chloride concentration in the interstitial water extracted under pressure during expeditions 372 and 375. Here, we used n = 15 (Figure 3).

2.2.2. Resistivity-Derived Porosity

We determined resistivity-derived porosity at Site U1520 using the resistivity model for clay-rich sediments proposed by Revil et al. (1998) that provided satisfying results for input siliciclastic sediments from the Nankai (Bourlange et al., 2003; Conin et al., 2011) and North Sumatra (Dutilleul et al., 2020) margins. This model is based on Archie's (1942) law that links the resistivity-derived porosity ϕ to the formation factor $F = a\,\phi^{-m}$ where $1 \le m \le 3.5$ (Conin et al., 2011) and $a \sim 1$. Assuming Bussian (1983) and Bourlange et al.'s (2003) hypotheses since $\xi = \frac{\sigma_s}{\sigma_{if}} \ll 1$ at Site U1520, F can be expressed as follows:

$$F = \frac{\sigma_{if}}{\sigma}\left[1 + 2\xi\left(\frac{\sigma_{if}}{\sigma} - 1\right)\right]. \quad (6)$$

This model accounts for the high electrical surface conductivity σ_s that characterizes clay-rich siliciclastic sediments (Units I–III) and altered volcaniclastics (Units V and VI) where primary volcanic glass or minerals have been replaced by secondary aluminosilicates (clays, zeolites) (Revil, 2002; Soueid Ahmed et al., 2018). In such clay-rich material, σ_s depends on electrical conduction in the double layer (i.e., Stern and diffuse layers) coating the surface of the grains and is determined from CEC (Revil, 2002). The model proposed by Revil et al. (1998) assumes a major contribution of the Stern layer to surface electrical conduction, spherical grains (i.e., the tortuosity $F\phi$ equals 3/2) and a linear temperature dependency of the exchangeable cation mobility β_s:

$$\sigma_s = \frac{2}{3}\rho_s\, CEC\, \beta_s. \quad (7)$$

The bulk electrical conductivity σ was obtained using a combination of LWD and wireline resistivity data. The electrical conductivity of the interstitial fluid σ_{if} was calculated from the concentration of Cl^-, Na^+, K^+, Ca^{2+}, Mg^{2+}, and SO_4^{2} in interstitial water (C^i_{iws}) and seawater (C^i_{sw}), the ionic mobility in the fluid β^i_f and Z_i the number of charges of ions given by Revil et al. (1998), and σ_{sw} the sea water conductivity

$$\sigma_{if} = \sigma_{sw} \frac{\sum_i \left(\beta_f^i \times Z_i \times C_{iws}^i\right)}{\sum_j \left(\beta_f^i \times Z_j \times C_{sw}^j\right)}, \tag{8}$$

$$\text{with } \sigma_{sw} = 5.32(1 + 0.02(T - 25)), \tag{9}$$

$$\text{and } T(°\text{C}) = 0.4 + 38.0 \times 10^{-3} z, \tag{10}$$

at Site U1520 (Barnes et al., 2019).

2.3. Pore-Network Characterization

Pore structure was characterized using NMR, MICP, and low-pressure nitrogen gas adsorption (N_2GA) that investigate complementary pore size ranges. We use the International Union of Pure and Applied Chemistry (IUPAC) nomenclature (Sing et al., 1985) to classify pores based on their diameter size as macropores (>50 nm), mesopores (2–50 nm), and micropores (<2 nm). All the samples were analyzed using NMR; 48 were also analyzed using MICP. Six of the samples showing an MICP pore size distribution dominated by mesopores and potentially micropores were selected for N_2GA. Pore-size distribution obtained by NMR, MICP, and N_2GA were finally compared and combined to obtain a more reliable distribution of micropore to macropore size distribution (e.g., Daigle, 2014; Schmitt et al., 2013).

2.3.1. MICP

MICP was performed at room temperature (20°C) on 2–4 cm^3 samples that were previously oven-dried at 105°C ± 5°C for 24 hr. The measurements were carried on using a Micromeritics® AutoPore IV 9500 and includes a low-pressure analysis and a high-pressure analysis. During the low-pressure analysis, the sample is degassed under vacuum. Then, the mercury fills the penetrometer, and the intruded volume is gradually measured up to a mercury pressure of ~0.2 MPa. The high-pressure analysis consists in stepwise measurements of the volume of intruded mercury during (1) an intrusion stage up to a maximum mercury injection pressure of 220 MPa, (2) an extrusion stage where pressure decreases down to atmospheric pressure, and (3) a reintrusion stage by increasing pressure up to the maximum value. The range of mercury injection pressure (0–220 MPa) allows to investigate macropore and mesopore throat diameters distribution from 360 μm to 5.7 nm using the Young-Laplace equation:

$$r = \frac{2\,\sigma_{Hg} \cos\theta_{Hg}}{P_{Hg}}, \tag{11}$$

where r is the pore throat radius (m), σ_{Hg} is the air-mercury interfacial tension (0.485 N/m), θ_{Hg} is the mercury-sediment contact angle (140°), and P_{Hg} is the mercury injection pressure (Pa).

The three-stage high-pressure analysis allows to determine mercury total connected porosity, mercury-free porosity, and mercury-trapped porosity (Rosener & Géraud, 2007). Mercury-total connected porosity is measured during the first intrusion stage as the mercury fills the connected pore space with increasing mercury injection pressure. At the end of the extrusion stage, some mercury droplets remain trapped in pores with narrow throats (i.e., pores with throats at least seven times narrower than pore bodies according to Li & Wardlaw 1986), allowing to determine the mercury-trapped porosity which can be used as a proxy for pore compaction. Finally, during the reintrusion stage, only the mercury-free porosity is intruded. MICP pore throat size distribution was used to determine the Katz-Thompson permeability K_{KT} (Katz & Thompson, 1986, 1987; Nishiyama & Yokoyama, 2014):

$$K_{KT} = \frac{1}{89} \phi_i \frac{\left(l_{max}^h\right)^3}{l_c} f\left(l_{max}^h\right), \tag{12}$$

with l_c the pore throat diameter corresponding to the inflection point of the cumulative MICP curve $f(l)$ of fractional volume of connected pore throats having diameters of l and larger, l_{max}^h the pore throat diameter corresponding to the optimum path for permeability obtained when $l^3 f(l)$ reaches its maximum value ($l = l_{max}^h$) (Katz & Thompson, 1986, 1987).

2.3.2. NMR

Proton NMR consists in monitoring the magnetization of the hydrogen nuclei of water molecule with static and pulsed magnetic fields (Daigle et al., 2014; Dennis, 1997; Dunn et al., 2002; Grunewald & Knight, 2009; Vincent et al., 2011). It first involves the equilibrium alignment of the hydrogen nuclei with a static magnetic field B_0 generated either by a logging or laboratory tool. Then, a secondary pulsed magnetic field B_1 is emitted at a specific radio frequency to perturb the system. B_1 is removed to measure the time required for hydrogen nuclei to relax to their original equilibrium alignment to B_0 through diffusion and interaction with the porous media. Commonly, the characteristic time measured is the relaxation in a plane perpendicular to B_0, referred to as the transverse relaxation time T_2 (seconds). T_2 provides information about pore structure in sedimentary rocks, including pore size distribution and porosity (Daigle et al., 2014). NMR measurements were performed using Bruker® Minispec Mq20 (20 MHz) and Mq10 (10 MHz) at room temperature (20°C) and atmospheric pressure on saturated core samples with a diameter of 8 mm and samples of ~5–8 cm^3, respectively. The magnetization decay was measured using the Carr-Purcell-Meilboom-Gill (CPMG) pulse sequence (Carr & Purcell, 1954; Meiboom & Gill, 1958) that consists of an initial $\pi/2$ magnetic field pulse orthogonal to B_0 separated by a time τ from a series of π pulses applied with opposite polarity at regular interval 2τ. We used a recycle delay of 0.1 s and a half-echo time τ of 0.04 ms (the minimum available for this equipment), a gain ranging 70–80%, 200 echoes per scan, and 128 scans were stacked.

We used UpenWin© software to inverse stacked magnetization decay data in a smoothed T_2 distribution. We determined the volume of water V_w in the sample to calculate NMR porosity as suggested by Daigle et al. (2014):

$$\phi_{NMR} = \frac{V_w}{V_w + V_s}. \tag{13}$$

V_w is determined using a calibration where the maximum signal amplitude A_0 (corrected for the gain) is recorded during the T_2 measurement for known volumes of water: $V_w = 19.762 * A_0 - 0.092$ ($R^2 = 0.94$). NMR T_2 distribution and MICP pore throat size distribution were correlated following Marschall et al. (1995) using the relation

$$T_2 = \frac{1000r}{2\,\rho_e}, \tag{14}$$

where T_2 is in milliseconds, r is pore throat radius in micrometer, and ρ_e is the effective relaxivity in micrometer per second.

2.3.3. Nitrogen Gas Adsorption (N_2GA)

Nitrogen adsorption/desorption isotherms were measured at 77 K at the LIEC laboratory in Vandoeuvre-lès-Nancy, France, using a BEL Japan BELSORP-mini II with pressure sensors ranging 0–133 kPa. Samples were dried for 24 hr at 105°C ± 5°C and then crushed, before being first outgassed at 30°C for 12 hr under vacuum. Adsorbed nitrogen gas volume and equilibrium relative pressure P/P_0 (where P is the gas equilibrium pressure and P_0 is the vapor saturation pressure) were measured at 77 K as P/P_0 increases up to 0.98 (adsorption isotherm) and decreases (desorption isotherm) stepwise. Adsorption isotherm shape and hysteresis loop were interpreted following the IUPAC (Sing et al., 1985) and De Boer (1958) classifications, respectively. Adsorption isotherm shape provides insights on pore sizes and volume while the type of hysteresis characterizes the geometry of pores. The amount of adsorbed gas at low P/P_0 is correlated with micropore and fine mesopore volume while it is related to large mesopore and macropore volume near $P/P_0 = 1$ (Labani et al., 2013). Adsorption/desorption isotherms were also used to characterize pore size distributions for small macropores and mesopores ranging 2.8–80 nm and specific mesopore volume using the Barrett-Joyner-Halena (BJH) method assuming cylindrical shape for pores to be consistent with MICP. Specific micropore volume and external surface area were determined using the De Boer (t-plot) model. Specific surface area was determined using the Brunauer-Emmett-Teller (BET) method. Nitrogen porosity ϕ_{N_2} was determined from the bulk density ρ_b (g/cm^3) and the specific pore volume V_{sp} (cm^3/g) (e.g., Labani et al., 2013):

$$\phi_{N_2} = \rho_b V_{sp}. \quad (15)$$

2.4. Bulk and Clay Mineralogy

We generally used the mineral composition given by shipboard XRD data that gives the relative abundance of total clay minerals, quartz, feldspar, and calcite normalized to 100% and document the occurrence of other minerals. To get supplementary information about the composition of hydrous minerals (type of clays and zeolites) on volcaniclastic samples from Units V and VI, additional post-cruise XRD analyses were carried on using a Bruker® D2 Phaser diffractometer operating at 30 kV and 10 mA with a Cu Kα radiation on bulk powder and <2 μm clay fraction. Bulk powder (respectively <2 μm clay fraction) samples were scanned between 2° and 70° (respectively 3–40°) with a step size of 0.02° and a time per step of 0.60 s (respectively 1.0 s) to determine the relative mineralogy using Bruker® EVA software. The relative abundance of calcite from XRD was compared to the abundance of calcite measured using an OFITE® Calcimeter (similar to Karbonat-Bombe) on the same sample. The <2 μm clay fractions were prepared following Thiry et al.'s (2013) procedure to make oriented deposits that provide information about clay mineralogy and non-oriented deposits that give further details about the type of kaolinite, illite, or smectite using the d(060) ray (Holtzapffel, 1985). Oriented deposits underwent a three-stage treatment (Thiry et al., 2013) and were scanned after each stage between 3° and 40° with a step size of 0.02° and a time per step of 1.0 s. The treatment includes (1) a 12 hr drying stage at room temperature, (2) a 24 hr stage of saturation with ethylene glycol under confining atmosphere, and (3) a heating cycle in a convection oven up to 490°C.

3. Results

3.1. CEC and Mineral Composition

Shipboard XRD data show that siliciclastic Units I to III are characterized by ~43% of clay minerals (Figure 2d) and relatively low CEC ranging 0.09–0.19 mol/kg (Figure 2e). This range of CEC values evidences that clay minerals are mainly kaolinite and/or illite and/or chlorite. Unlike Units I–III, carbonate Unit IV is characterized by strong variations of mineral composition depending on lithology. In the upper part of the unit that is mainly composed of marls, total clay content shows a general trend that increases with depth from ~20% up to 55%. In underneath chalks, total clay content decreases with depth from ~20% in muddy chalks to only a few percent in clear chalks. Calcimetry values vary from 23% to 63% in marls and from 64% to 93% in chalks (Figure S1) and are in good agreement with shipboard and post-cruise XRD measurements of calcite content. CEC increases from very low values ~0.06 mol/kg at the top of the unit to moderately high values up to ~0.30 mol/kg in the deepest marls where debris flow deposits occur, with moderate values ~0.16 mol/kg in the calcareous mudstone interval sandwiched in between. In underneath chalks, it is very constant and low, averaging ~0.04 mol/kg. XRD shows that clay minerals are largely dominated by dioctahedral two-water layer smectites, explaining the relatively high CEC values obtained although calcite content is high. Some illites are also present. Volcaniclastic Units V and VI are characterized by strong variations of facies over centimeter to decimeter length scales (Barnes et al., 2019, 2020), including changes in hydrous minerals distribution and local occurrence of fractures, calcite veining, and cement, changes in texture, clast shape, size, and alteration degree. Shipboard XRD measurements show that clay content scatters from 20% to 95% and is inversely correlated with calcite content that ranges 1–76%. Post-cruise calcimetry shows that calcite content varies from 1% to ~43% in volcaniclastic conglomerates, from 23% to 72% in marls, and ~2% in siliceous mudstones (Figure S1). These results are in the same order than post-cruise XRD but may differ from shipboard XRD that tend to overestimate calcite content by accounting only for calcite, quartz, feldspar, and clays even in samples with significant amount of other minerals like zeolites. These strong mineralogical variations result in very scattered CEC that ranges 0.23–0.88 mol/kg in volcaniclastic conglomerates from Units V and VI, 0.12–0.46 mol/kg in marls, and 0.32–0.84 mol/kg in siliceous mudstone from Unit VI. In volcaniclastic Units V and VI, high CEC values and post-cruise XRD measurements show that clay minerals are mainly two-water layer dioctahedral smectites with only minor amounts of illite and chlorite (Figure S2), except in the lower part of Unit VI where significant amount of illite occur in basalt. XRD also reveals that zeolite minerals are common in conglomerates with phillipsite occurring in most of the samples while heulandite or clinoptilolite was found only in Unit VI samples (Figure S2). Amorphous fraction is relatively high ranging 29–41% due to the occurrence of amorphous opal or volcanic glass. Overall, at Site U1520,

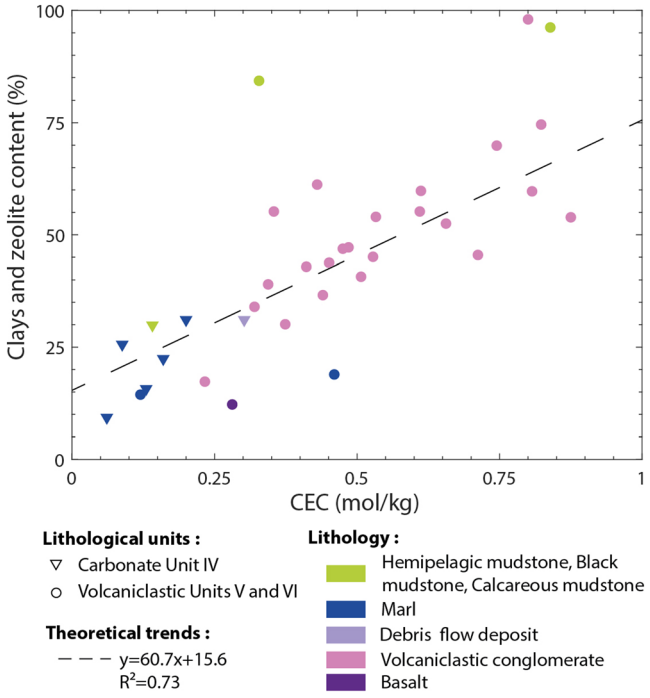

Figure 4. Relation between total clay and zeolite contents measured by XRD in this study and cation exchange capacity per unit and lithology.

CEC increases with hydrous mineral content (Figure 4) and reciprocally decreases with non-hydrous mineral content that are mainly quartz, feldspar, or calcite (Figure S1a) depending on the unit (Figure 2c).

3.2. Total Connected Porosity

Total connected porosity shows extreme variations across Site U1520 with specific patterns for each and within each lithologic unit (Figure 2f). It exponentially decreases with depth from ~72% at the top of Unit I to ~46% at the bottom of Unit III. Total connected porosity shows different trends across carbonate Unit IV. In the interval dominated by marls, total connected porosity is relatively homogeneous and constant at ~47% from ~510 to ~610 mbsf, decreases up to ~42% in the ~610–690 mbsf interval despite exhibiting a wide scatter from 34% to 55% and remains scattered (28–42%) but relatively constant at ~33% up to 776 mbsf. In underneath chalks, total connected porosity steadily increases up to ~45%. Total connected porosity does not show any specific pattern in volcaniclastic Units V and VI where it is extremely scattered from 20% up to 56% and anti-correlated with *P* wave velocity that also strongly varies from 1,800 to 5,000 m/s (Barnes et al., 2020). However, in these units, total connected porosity globally linearly increases with CEC (Figure 5) and pore size (Figure S3a) and decreases with calcite content (Figure S1b), with specific trends depending on lithology. In particular, siliciclastic samples from Units I–III, chalks and shallow marls (~510–690 mbsf) from Unit IV are characterized by a low CEC (<0.2 mol/kg) that is not correlated to total connected porosity. On the contrary, Unit IV clay-rich marl interval (~690–776 mbsf), volcaniclastic conglomerates, siliceous mudstones, and marls from Units V and VI are characterized by higher CEC values that are correlated with total connected porosity.

3.3. Bound Water Content

Extreme variations of CEC across Site U1520 sedimentary section results in contrasted bound water content (Figure 2f). In siliciclastic Units I–III, the low and homogeneous CEC content causes very constant and low bound water content that averages ~5%. In contrast, CEC variations across carbonate Unit IV results in heterogeneous moderate bound water content that increases with depth from ~2% to 15% in marls while it is only ~2% in chalks. CEC being even more scattered in volcaniclastic Units V and VI, bound water content shows strong variations from moderate to very high values, averaging ~22% in conglomerates, ~17% in siliceous mudstones, and ~7% in marls.

3.4. Interstitial Porosity

Similar to the total connected porosity data, interstitial porosity data globally exponentially decreases with increasing depth through siliciclastic Units I–III, from ~70% near the seafloor to ~40% at the bottom of Unit III (Figures 2f and 2j). Corresponding compaction curves are $\phi_i = 46.6e^{-0.029\,\sigma_v'}$ ($R^2 = 0.29$) where σ_v' is effective vertical stress in MPa and $\phi_i = 46.6\,e^{\left(-\frac{z}{4144}\right)}$ ($R^2 = 0.27$) where z is depth in mbsf. Coarser sand-rich packages from Unit I are slightly more compacted than the global compaction trend, evidencing a particle-size dependency of compaction. In carbonate Unit IV, total connected porosity and interstitial porosity both show similar variations but the latter are intensified for interstitial porosity. In marls, interstitial porosity decreases from ~50% to ~39% up to ~690 mbsf and remain relatively constant ~25% through the lower part of the interval where debris flow occurs. In chalks, it steadily increases up to ~46%. The ~690–848 mbsf interval where interstitial porosity is preserved in marls and chalks correspond to a higher *P* wave velocity and thermal conductivity zone (Barnes et al., 2019). Several zones where interstitial porosity locally drops in marls are correlated to fault zones (Figure 2k; 660–670 and 690–700 mbsf). Another fault zone occurs at the marls/chalks boundary (~770 mbsf). As a result of Units V and VI high bound water content, interstitial porosity is significantly lower than total connected porosity and scatters between 3% and

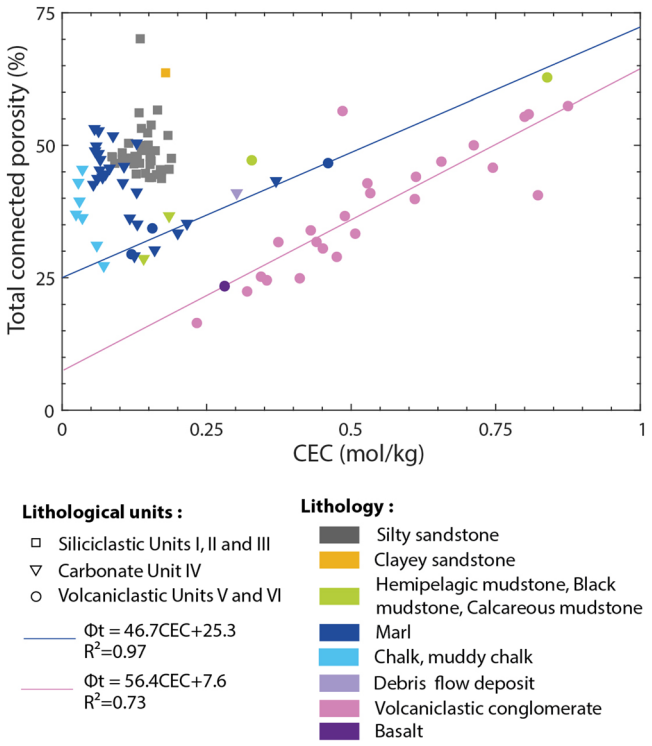

Figure 5. Total connected porosity versus cation exchange capacity for 106 samples from Site U1520 per lithological units and detailed lithology. The navy solid line corresponds to the best-fit trend for marls samples from Unit V. The pink solid line corresponds to the best-fit trend for volcaniclastic conglomerates samples from Units V and VI.

44% in conglomerates. The lowest values occur in calcite cemented samples with high *P* wave velocity (Barnes et al., 2019), and the highest values occur in poorly consolidated, matrix-supported altered conglomerates with elevated clay fraction. Interstitial porosity also strongly varies in Unit V marls and Unit VI siliceous mudstones.

3.5. LWD and Wireline Porosity: NMR, Neutron, and Resistivity-Derived Porosity

In Units I–III, neutron and NMR LWD porosity data are nearly equal and generally exceed total connected porosity (Figure 2f). The exceedance decreases as depth increases so that both nearly fit total connected porosity data below the coring gap in Unit III. In the Unit IV interval where NMR and neutron porosity logs are available, total connected porosity scatters between NMR and neutron porosity values. In the marl interval with high CEC values and thus high total clay content, LWD NMR better fits interstitial porosity rather than total connected porosity. NMR LWD porosity data fit very well to NMR porosity measured on samples.

Resistivity-derived porosity shows a behavior similar to that of interstitial porosity across the sedimentary column using the model developed by Revil et al. (1998) for clay-rich material by increasing Archie's law parameter m with increasing depth and using $a = 1$ (Figure 2j). A suitable match was obtained with $m = 1.9$ in Units I–III and $m = 2.3$ in Unit IV and in the upper part of Unit V where wireline resistivity was locally acquired. Cementation factors ~2 are commonly obtained for siliciclastic clay-rich facies (e.g., Bourlange et al., 2003; Conin et al., 2011; Dutilleul et al., 2020). It can be noticed that resistivity-derived porosity is consistent with interstitial porosity in carbonate Unit IV, although clay content significantly varies in this interval from zero to moderate values. Reciprocally, in volcaniclastic Unit V, resistivity-derived porosity matches very well interstitial porosity data contrary to total connected porosity data.

3.6. Pore Structure

3.6.1. MICP

In Units I to IV, MICP shows that there is only one family of macropore throats (Figure 2g). In siliciclastic Units I–III, the average diameter d_{50} of macropore throats is heterogeneous and ranges 0.2 to 0.7 μm. It is well correlated to interstitial porosity and total connected porosity with $\phi_i = 19.5 * d_{50} + 34.75$ ($R^2 = 0.62$) and $\phi_t = 18.6 * d_{50} + 40.78$ ($R^2 = 0.60$), the largest throats corresponding to the most porous samples (Figures S3a and S3b). In marls from Unit IV, the average diameter of macropore throats becomes more homogeneous and strongly decreases with increasing depth, from ~0.3 μm at the top of the unit to ~65 nm for the deepest marls. It is well correlated to interstitial porosity and total connected porosity with $\phi_i = 98.7 * d_{50} + 18.7$ ($R^2 = 0.92$) and $\phi_t = 54.5 * d_{50} + 32.5$ ($R^2 = 0.70$) (Figures S3a and S3b), the largest throats corresponding to the most porous samples. In contrast, in chalks, the average diameter of macropore throats is very homogeneous and slightly increases with depth from ~0.2 to ~0.4 μm. In volcaniclastic Units V and VI, most conglomerates exhibit a unimodal MICP pore throat size distribution with a dominant heterogeneous family of mesopore throats (2 nm $< d_{50} <$ 20 nm). However, few samples are characterized by bimodal MICP pore throat size distribution and also show a secondary family of macropores throats (2 μm $< d_{50} <$ 30 μm) accounting for ~25% of the porosity. The average diameter of the main family of mesopores is also correlated to interstitial porosity and total connected porosity with $\phi_i = 1455.9 * d_{50} + 1.2$ ($R^2 = 0.34$) and $\phi_t = 1641.5 * d_{50} + 22.1$ ($R^2 = 0.33$). In contrast, marls and siliceous mudstones are characterized by one family of mesopore to macropore throats ranging 6–640 nm in marls and 8–40 nm in siliceous mudstones. Mercury-trapped porosity follows the evolution of total connected porosity. The Katz-Thompson permeability (Figures 2h and S3c) was determined based on the dominant family of pore throats determined by MICP and follows the evolution of their diameter. It globally decreases with depth from ~$2.0 \cdot 10^{-16}$ m^2 to

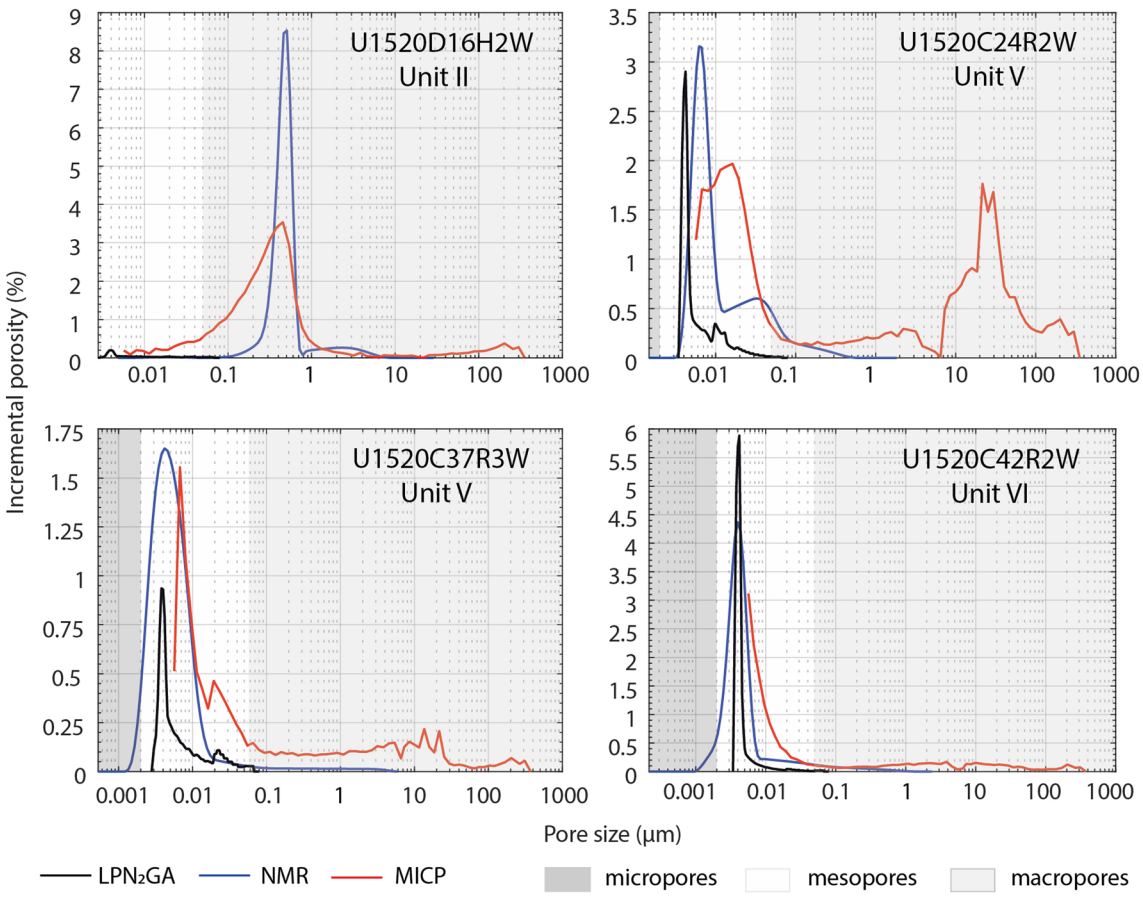

Figure 6. Comparison of pore size distributions from MICP, N_2GA (cylindrical BJH model), and converted NMR for representative samples from siliciclastic Unit II and volcaniclastic Units V and VI.

~$1.8{\cdot}10^{-17}$ m^2 in siliciclastic Units I to III and from ~$5.1{\cdot}10^{-17}$ to ~$1.9{\cdot}10^{-18}$ m^2 in the marl interval from Unit IV and increases from ~$1.9{\cdot}10^{-17}$ to $1.9{\cdot}10^{-16}$ m^2 in the chalk interval. Units V and VI are characterized by heterogeneous permeability values that range $4.7{\cdot}10^{-19}$ to ~$2.2{\cdot}10^{-17}$ m^2 in marls, ~1.7–$3.8{\cdot}10^{-19}$ m^2 in siliceous mudstones, ~$2.2{\cdot}10^{-20}$ m^2 in basalt and that are in the order of ≤$1.0{\cdot}10^{-20}$ to $2.0{\cdot}10^{-19}$ m^2 in unimodal volcaniclastic samples. The five volcaniclastic samples showing bimodal MICP pore throat size distribution (Figures 2g and S4) are characterized by a mesoporal Katz-Thompson permeability in the ~1–$2{\cdot}10^{-19}$ m^2 range of values and significantly higher macroporal Katz-Thompson permeability in the order of 10^{-16} to 10^{-13} m^2. However, from our data, we were not able to discriminate which family of pores drives bulk permeability (Lai & Wang, 2015; Nooruddin et al., 2014; Rosenbrand et al., 2015; Zhao et al., 2015). Hence, we assume that, for these samples, permeability ranges between mesoporal and macroporal permeability and thus consider both endmembers in section 4.

3.6.2. NMR

In siliciclastic Units I–III, the distribution of NMR T_2 measured on samples is characterized by a major T_2 peak ~1.6–5.3 ms at 10 MHz and ~3.0–0.7 ms at 20 MHz (Figure 2i) corresponding to interstitial water that is often negatively skewed, eventually associated with a minor peak occurring <0.1 ms interpreted as bound water (Cheng & Heidari, 2017; Ellis & Singer, 2007; Yuan et al., 2018) (Figure 6). LWD T_2 distribution differs from laboratory data with an average T_2 that decreases from ~100 ms at the top of Unit I to ~10 ms at the bottom of Unit III. MICP and NMR can be correlated using an effective relaxivity ρ_e ranging 18–53 μm/s (in average, 35 μm/s, excluding the high value ~296 μm/s) at 10 MHz and ranging 23–62 μm/s (in average, 38 μm/s, excluding the high value ~407 μm/s) at 20 MHz, as found by Daigle et al. (2014) for equivalent lithologies. Lower effective relaxivity ~6 μm/s must be used to fit the higher LWD T_2 to MICP measurements on samples. In Unit IV, variations of the average T_2 are correlated to that of pore throat size measured by

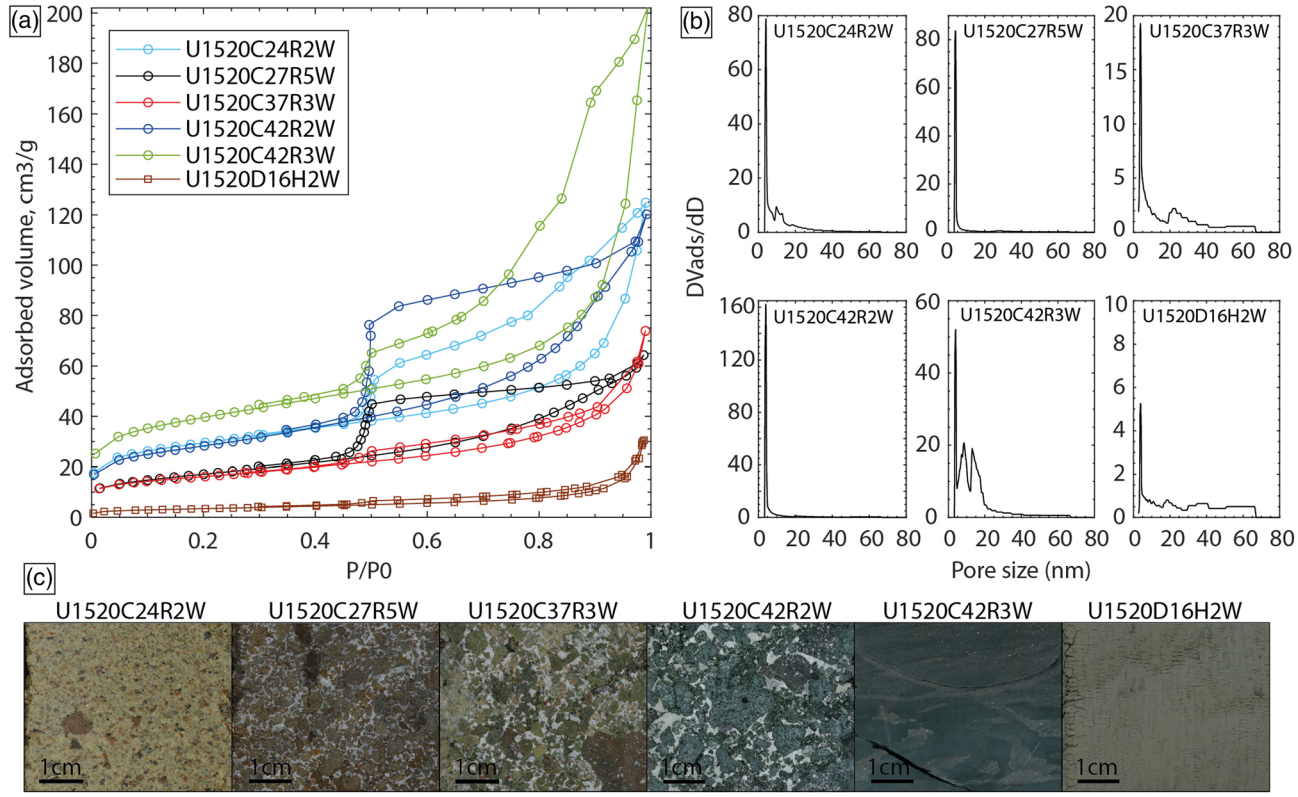

Figure 7. (a) Adsorption-desorption N_2 isotherms at 77 K and (b) distribution of the size of mesopores (2–50 nm) and small macropores (>50 nm) obtained with the BJH method assuming cylindrical pores for (c) representative samples from siliciclastic Unit II (U1520D16H2W) and volcaniclastic Units V (U1520C24R2W, U1520C27R5W, and U1520C37R3W) and VI (U1520C42R2W and U1520C42R3W).

MICP. T_2 decreases from up to ~4.7 ms (respectively, 3.6 ms) at the top of the unit to ~0.3 ms (respectively, 1 ms) at the bottom of the marl interval at 10 MHz (respectively, 20 MHz). In chalks, T_2 slightly increases with depth from ~0.6 ms up to ~5.5 ms at 10 MHz and from ~3.0 ms to ~5.1 ms at 20 MHz. The discrepancy between T_2 measured on samples and LWD T_2 is strongly reduced in Unit IV although LWD NMR is available only in a limited section of the upper marl interval. There, LWD T_2 decreases from ~10 to ~2 ms. At 10 MHz, effective relaxivity ranges 18–106 μm/s in marls (in average, 51 μm/s) and ~83–45 μm/s in chalks (in average, 64 μm/s). At 20 MHz, it ranges 15–28 μm/s in marls (in average, 21 μm/s) and ~15–19 μm/s in chalks (in average, 17 μm/s). LWD effective relaxivity averages 13 μm/s in marls and ~31 μm/s in chalks. In volcaniclastic Units V and VI, NMR T_2 distribution either show unimodal or bimodal positively skewed T_2 distribution with a major peak ranging 0.5–1.7 ms at 10 MHz. This peak corresponds to the major family of mesopores observed on MICP with ρ_e ranging 1.4–7.3 μm/s (in average, 2.6 μm/s) (Figure 6). Unit V marls and Unit VI siliceous mudstones are characterized by unimodal T_2 distributions with relatively narrow peaks in siliceous mudstones and positively skewed peaks in marls with modes ~1.5–2 ms. These T_2 peaks correspond to the mesopores to macropores evidenced by MICP using ρ_e ranging 5.3–54.7 μm/s (in average, 26 μm/s) in marls and ρ_e ~3.2 μm/s in siliceous mudstones.

3.6.3. N_2GA

Adsorption-desorption isotherms for siliciclastic Units I–III and volcaniclastic Units V and VI samples are type II isotherms with type B hysteresis (De Boer, 1958) evidencing macropores and mesopores with slit shape (Figure 7) as typically observed in clay-rich sediments (e.g., Daigle, 2014; Labani et al., 2013). Unlike siliciclastic samples, most volcaniclastic samples show hysteresis loops with steep desorption branches that suggest high-aspect ratio pores due to parallel alignment of clay mineral particles (Janssen et al., 2011, and references therein). Specific surface area (Table 1) is significantly higher in volcaniclastic

Table 1
Summary of Porosity Data for Representative Samples From Siliciclastic Unit II (U1520D16H2W) and Volcaniclastic Units V (U1520C24R2W, U1520C27R5W, and U1520C37R3W) and VI (U1520C42R2W and U1520C42R3W) where ϕ_t is Total Connected Porosity, ϕ_i is Interstitial Porosity, ϕ_b is Bound Water Content, ϕ_{N_2} is N_2GA Porosity, ϕ_{Hg} is MICP Porosity, $\phi_{N_2} + \phi_{Hg}$ Corrected is the Porosity Derived From the Combination of the Pore Size Distributions From N_2GA (<80 nm) and MICP (>80 nm), ϕ_{NMR} is NMR Porosity, ϕ_{micro} and ϕ_{meso} are Microporosity and Mesoporosity Derived From N_2GA Using the Cylindrical BJH Model and ϕ_{macro} is Remaining Macroporosity, and S_{spe} is the BET Surface Area

	Type of porosity (%)										
Sample	ϕ_t	ϕ_i	ϕ_b	ϕ_{N_2}	ϕ_{Hg}	$\phi_{N_2} + \phi_{Hg}$ corrected	ϕ_{NMR}	ϕ_{micro}	ϕ_{meso}	ϕ_{macro}	S_{spe} (m^2/g)
U1520D 16H2W	47.9	42.3	5.6	7.5	38.3	43.4	56.3	0.1 (0%)	7.4 (17%)	35.9 (83%)	12.3
U1520C 24R2W	55.4	29.7	25.7	32.9	39.5	53.6	43.7	2.5 (5%)	30.4 (57%)	20.7 (38%)	106.6
U1520C 27R5W	33.9	13.3	20.6	19.8	8.4	22.4	—	0.8 (4%)	19.0 (85%)	2.6 (11%)	61.1
U1520C 37R3W	24.9	2.6	22.3	21.8	11.8	26.1	—	1.2 (5%)	20.6 (79%)	4.3 (16%)	58.1
U1520C 42R2W	40.6	5.9	34.7	34	16.2	56.4	—	1.7 (3%)	32.3 (57%)	22.4 (40%)	101.5
U1520C 42R3W	62.8	40.78	22.0	46.4	40.2	49	63.7	2.1 (4%)	44.3 (90%)	2.6 (6%)	143.4

samples (~58–143 m^2/g) characterized by a majority (57–90%) of small mesopores and macropores (11–40%) than in siliciclastic samples (~12 m^2/g) that are mostly composed of macropores (>80%).

4. Discussion

4.1. Relation Between CEC, Hydrous Mineral Composition, and Bound Water Content

Although post-cruise measurements were carried on different pieces of samples from heterogeneous Units V and VI, there are clear trends relating CEC and bulk mineral composition (Figures 2, 4, and S1a) evidencing that CEC is a sensitive proxy for bulk bound water content (Figure 3). Scattered CEC values from Unit I to VI reflect the evolution of the ratio of non-hydrous to hydrous mineral content and the type of hydrous mineral since non-hydrous minerals all show very low theoretical CEC values whereas hydrous minerals are characterized by specific theoretical high to very high CEC values. Theoretical CEC is 0.8–1.5 mol/kg in pure smectite, 0.1–0.4 mol/kg in illite, ~4.5 mol/kg in phillipsite, ~3.2 mol/kg in heulandite, ~2.2 mol/kg in clinoptilolite, and 0.08–0.13 mol/kg in opal (e.g., Derkowski et al., 2015; Pabalan & Bertetti, 2001; Reeves et al., 2006). Here, non-hydrous minerals are mainly quartz and feldspar in siliciclastic Units I to III and calcite in Units IV to VI. Hydrous minerals are mostly smectites in all samples, with zeolites occurring in some conglomerates from Units V and VI and opal in siliceous mudstones from Unit VI. XRD data evidence that from Unit I to VI, smectites are dioctahedral two-water layer smectites with d(0001) ranging 14.6–15.5 Å and a d(060) value ~1.50 Å. This supports the fact that most data plot on a bound water ratio-CEC trend that corresponds to $n = 15$ water molecules per cation charge (Figure 3). We relate the scatter of the data around this trend by the occurrence of other hydrous minerals like zeolites and opal that theoretically show higher and lower CEC than smectite, respectively.

4.2. Controls on Porosity

The absence of correlation between CEC and total connected porosity for Units I–III (Figure 5), shallow marls (~510–690 mbsf), and chalks from Unit IV shows that for these lithologies, total connected porosity is mainly controlled by compaction rather than mineralogy. This is also evidenced by the linear decrease of macropore size with decreasing total connected porosity that characterizes samples from Units I–III and marls from Unit IV (Figure S3a). From siliciclastic Unit I to ~690 mbsf in Unit IV marl interval, interstitial porosity and resistivity-derived porosity exhibit a normal consolidation trend as typically observed in the shallow parts of the basins entering subduction zones (e.g., Dutilleul et al., 2020; Kitajima & Saffer, 2014; Screaton et al., 2002). It is thus possible to use this trend as a reference compaction trend to compare with that of equivalent lithologies at other sites located closer to the deformation front. In chalks from Unit IV, the strong increase in pore throats diameter, interstitial porosity (Figures 2f and S3b), *P* wave velocity, and thermal conductivity (Barnes et al., 2019) suggests higher cementation that prevents pores from collapsing. On the other hand, samples with higher CEC values (>0.2 mol/kg) like the clay-rich marl interval with calcareous mudstones and debris flow deposits in Unit IV (~690–776 mbsf) and Units V and VI are characterized by a very good positive (respectively negative) correlation between CEC (respectively calcite

content) and total connected porosity (Figures 5 and S1b) and a positive correlation between calcite content and *P* wave velocity (Barnes et al., 2019). This evidences a strong control of the ratio of hydrous to non-hydrous mineral content on physical properties in these units. In volcaniclastics, marls, and siliceous mudstones from Units V and VI, high hydrous mineral content results in elevated bound water content and thus enhanced total connected porosity, whereas high calcite content in calcite-cemented intervals showing higher *P* wave velocity tends to strongly reduce interstitial porosity and thus total connected porosity. In the −690 to 776 mbsf marl-rich interval in Unit IV, the small decrease in interstitial porosity and macropore size is correlated to increasing *P* wave velocity and high thermal conductivity values (Barnes et al., 2019) that suggest higher cementation with increasing depth. This effect is counterbalanced by a rise in clay bound water content with depth, resulting in relatively constant total connected porosity. There is also a relation between porosity and deformation in marls from Unit IV since fault zones occur in zones (660–670 mbsf; 690–700 mbsf) where porosity is locally reduced in locally strengthened sediments with higher *P* wave velocity (Barnes et al., 2019).

4.3. Comparison of Logging Porosity and Porosity Measured on Samples

The very good match of resistivity-derived porosity to interstitial porosity across the entire sedimentary section and underlying oceanic crust supports hypotheses raised in previous works. First, resistivity-derived porosity must be calibrated using effective porosity like interstitial porosity rather than total connected porosity (e.g., Conin et al., 2011), suggesting that bound water cannot be recorded at the scale of resistivity logs here although it is commonly assumed (e.g., Ellis & Singer, 2007). Second, it is critical to account for the very high surface conductivity of clays in siliciclastic clay-rich (e.g., Bourlange et al., 2003; Conin et al., 2011) and altered volcaniclastic clay-rich materials (e.g., Revil, 2002) to accurately determine effective porosity from logging data.

Because of the truncation of NMR T_2 distribution between 1 and 1,000 ms, NMR logging data were expected to underestimate bound water content (typically <1 ms) (Barnes et al., 2019) and thus to better match interstitial porosity than total connected porosity. However, in Units I–IV, LWD NMR provides significantly higher clay bound water content than CEC does, resulting in LWD NMR porosity that is closer to total connected porosity than to interstitial porosity. LWD NMR porosity follows the pattern of interstitial porosity only in the bottom part of the LWD interval. Overall, the discrepancy between LWD NMR porosity and total connected porosity decreases as LWD T_2 becomes closer to T_2 measured on core samples. However, the data highlight that logging NMR data are not directly comparable with laboratory data. This can be explained by distinct ranges of T_2 distribution due to strong contrast of frequency between the logging tool and the Minispec on one hand and to variations in processing on the other hand. Although LWD NMR porosity equals NMR porosity measured on samples, in most samples (Units V and VI potentially excepted as discussed below), the quantification of bound water content from CEC seems to be more realistic than that from LWD NMR because of the too high T_2 cutoff values used to separate clay-bound water and interstitial water on logging data (e.g., Cheng & Heidari, 2017; Ellis & Singer, 2007; Yuan et al., 2018).

4.4. Pore Size Distribution From MICP, N_2GA, and NMR

Taking into account that MICP, N_2GA, and NMR measure distinct features of pores and were performed on distinct pieces of samples picked up from heterogeneous formations, the three methods are very well correlated in the mesopore and small macropore (<10 μm) range of pore size distribution (Figure 6). In particular, the good match between N_2GA and MICP pore size distributions shows that MICP provides satisfying results when characterizing mesopores up to its detection threshold ~6 nm. Because of the parameters used for NMR experiments, NMR cannot capture macropores >10 μm. However, NMR pore size distribution satisfyingly averages the distribution resulting from MICP and N_2GA that provide information on the largest and smallest pores, respectively. This observation suggests that although N_2GA provides additional insights on microporosity and pore geometry, performing MICP and NMR experiments may be enough to characterize macropore to mesopore size distribution.

As suggested in previous works (e.g., Daigle, 2014; Schmitt et al., 2013), the porosity value obtained by combining N_2GA and MICP pore size distributions taking into account the range of overlap between both methods roughly equals total connected porosity (Table 1). Here, we show that this porosity better matches interstitial porosity for macroporous Unit II U1520D16H2W sample. However, for Units V and VI samples, it

significantly exceeds interstitial porosity, either suggesting that the producibility of fluids is not only related to pore size or that helium pycnometer may underestimate total connected porosity in mesoporous to microporous samples (e.g., Labani et al., 2013). Another possibility is that the occurrence of other hydrous minerals like opal or zeolites in addition to smectite in some samples from Units V and VI may lead to uncertainties regarding the determination of interstitial porosity with Equation 3 that is commonly used for sediments hosting clay only as hydrous minerals (Conin et al., 2011; Dutilleul et al., 2020; Henry, 1997; Henry & Bourlange, 2004).

4.5. Potential for Fluid Production

Our results suggest that siliciclastic Units I–III are characterized by a total connected porosity that is mainly controlled by compaction. These sediments are currently releasing interstitial water as a result of normal consolidation associated with burial and also have potential for bound water production associated with smectite dehydration at greater depth. In pelagic carbonate Unit IV, total connected porosity is affected by compaction, clay mineral content, and deformation processes associated with the generation of fault zones. In marls, there is a homogenization and reduction of pore size and a rise in total clay content with increasing depth. This suggests a reduction of the contribution of compaction to dewatering with ongoing lithification as depth increases while the potential for bound water production by smectite dehydration increases. In chalks, the increase in total connected porosity, interstitial porosity, and pore size may be induced by an increase in cementation that prevents pores from collapsing. In volcaniclastic Units V and VI, total connected porosity is mainly driven by bulk mineral composition. Conglomerates, siliceous mudstones, and marls are all characterized by elevated hydrous mineral content with significant potential for bound water production by dehydration of smectite, opal, and zeolite. Additional release of interstitial water may also occur in unconsolidated intervals like matrix-supported altered conglomerates.

4.6. Permeability, Flow Path, and Décollement Location

Permeability can be inferred from pore size distribution along the sedimentary section at Site U1520 with higher permeability expected in the intervals with larger pores at percolation threshold. The significant reduction and homogenization of macropore size from siliciclastic Unit I to carbonate Unit IV indicates a strong reduction of permeability that is mainly driven by pore collapse associated with vertical loading across this interval. In Unit IV, the lowest permeability (~10^{-18} m^2) occurs in the clay-rich marl interval ~690–776 mbsf with calcareous mudstone and debris flow deposits sandwiched in between. Beneath, chalks with larger macropores likely represent a more permeable (~10^{-17} to 10^{-16} m^2) interval above volcaniclastic Units V and VI characterized by contrasted hydrogeological properties. Units V and VI are globally characterized by very low permeability (~10^{-19} to 10^{-20} m^2) and dominant mesoporosity in calcite-cemented volcaniclastics, mudstones, or marls. The occurrence of calcite-filled veins in Units V and VI and chalks in Unit IV likely contributes to permeability reduction and suggests that fluid flow occurred in these units. The absence of such structures and the fact that no change in clay mineralogy was observed within and on both sides of the fault zones identified in the marl interval from Unit IV suggest that these fault zones do not act like preferential flow paths for fluids produced deeper. However, uncemented conglomerates showing both mesoporosity and macroporosity (e.g., sample U1520C24R2W in Figures 6 and 7) may form intervals of higher porosity and permeability channeling fluid flow, located at the top of Unit V or sandwiched in between calcite-cemented low-permeability mesoporous volcaniclastics that compose most of Units V and VI.

Along the margin, the décollement is thought to channel substantial fluids and to be highly overpressured (Barnes et al., 2010, and references therein; Ellis et al., 2015). At the southern part of the margin, it has been inferred from seismic data to coincide with or to lie about a hundred meters above seismic Reflector 7 (Barnes et al., 2010; Crutchley et al., 2020; Plaza-Faverola et al., 2012, 2016). Seismic Reflector 7 has been interpreted as the boundary between Miocene sediments and underlying Early Oligocene to Late Cretaceous low-permeability pelagic chalks and calcareous mudstones ("Sequence Y" of Davy et al., 2008). Beneath Sequence Y, Cretaceous sediments ("MES" sequence) and oceanic crust of the Hikurangi Plateau ("VB" sequence) have been identified (Crutchley et al., 2020; Davy et al., 2008). At Site U1520, the lower part of pelagic carbonate Unit IV and underlying volcaniclastic Units V and VI show similarity in terms of lithology to the "Y," "MES," and "VB" sequences described in the southern part of the margin. The lower part of Unit IV (seismic Unit 8, Figure 2a), Unit V, and the top of Unit VI show similar characteristics to that

developed at the locus for the formation of the future décollement at other subduction zones. In subduction zones, the décollement generally forms in overpressured fluid-rich and highly porous clay-rich zones correlated to high-amplitude negative polarity seismic reflection (Bangs et al., 1999, 2004; Cochrane et al., 1994; Dean et al., 2010; Mikada et al., 2005; Moore et al., 1998; Moore & Shipley, 1993; Shipley et al., 1994) and/or freshening anomalies associated with bound water release (e.g., Bekins et al., 1995; Dutilleul et al., 2020; Henry, 1997; Henry & Bourlange, 2004; Spinelli et al., 2006). At Site U1520, geophysical and geochemical signatures including local elevated bound water content related to high smectite, zeolite, and opal content, high amplitude-negative polarity seismic reflections (seismic Unit 9, Figure 2a) and freshening anomalies suggest that volcaniclastic Units V and VI are fluid-rich. In particular, three zones where interstitial water chloride content is ~6% less than modern seawater values occur at Site U1520 (Figure 2) ~769 mbsf in the lower part of pelagic carbonate Unit IV, ~875 and ~930 mbsf in volcaniclastic Unit V (Barnes et al., 2019). In Unit V, these chloride anomalies correspond to zones showing high total connected porosity and bound water content, but contrasted interstitial porosity values. They are also, at least locally, correlated to macroporous and mesoporous uncemented conglomerates expected to behave as pathways for fluids to flow. They have been interpreted shipboard as resulting from recent and local dehydration reactions. Possible rebuttals are the fact that shipboard pore water extraction process may result in anomalous freshening (Fitts & Brown, 1999) and the low in situ temperature ~40°C regarding the range of temperature required for dehydration reactions to occur (Barnes et al., 2019). The negative polarity seismic reflections typically suggest high fluid content (e.g., Dean et al., 2010) but may also be induced by the volcanic composition of rocks (Barnes et al., 2019). Although there are uncertainties regarding the present production of bound fluids and pore fluid pressure at Site U1520, volcaniclastic Units V and VI are very likely to produce fluids landward, at greater depth. The base of the smectite-rich marl interval in Unit IV where permeability is low may act as a barrier preventing the produced fluids from flowing toward the surface. In that case, this interval would accumulate elevated pore pressure and potentially behave like the locus for décollement initiation. Alternatively, the décollement may initiate at or below the carbonate Unit IV-volcaniclastic Unit V interface. If the hypothesis of uncemented volcaniclastic conglomerate intervals developing higher permeability (~10^{-13} to 10^{-16} m^2) associated with macroporosity is correct, then the interval of highly porous uncemented volcaniclastics occurring just below the Unit IV-Unit V interface and correlated to the chloride anomaly observed ~875 mbsf at Site U1520 would be a candidate for hosting trapped locally produced or deeper sourced fluids due to the contrast of permeability with upper Unit IV chalks (~10^{-16} to 10^{-17} m^2) and thus for developing elevated pore fluid pressure and for the décollement to initiate. Similarly, the décollement may initiate in zones of contrasted permeability in Units V or VI. There, the very low permeability characterizing mesoporous rocks that compose most of these units may act as a barrier preventing fluids to flow toward the seafloor, resulting in pore pressure buildup in higher porosity and permeability intervals hosting these fluids because of acting as preferential flow paths. A potential candidate is the interval corresponding to the chloride anomaly ~930 mbsf at Site U1520 where uncemented mesoporous and macroporous higher permeability conglomerates occur.

5. Conclusion

We have shown strong heterogeneities of interstitial and bound fluid contents, sediment compaction state, pore size distribution, and hydrous mineral content across the northern Hikurangi margin input section from IODP Expeditions 372/375 logging data and samples. We have evidenced the following:

1. Siliciclastic Units I–III are macroporous illite and smectite-bearing clayey siltstones to silty sandstones with low CEC and bound water content that currently undergo substantial compaction-induced dewatering as they are normally consolidated with burial.
2. Macroporous smectite-rich marls and calcareous mudstones with occasional debris flow deposits above chalks in the lower part of pelagic carbonate Unit IV might correspond to the locus for décollement initiation as suggested further south of the margin because of low permeability that may prevent fluids produced locally or deeper to flow toward the surface. Marls and calcareous mudstones undergo normal consolidation associated with a reduction of the size of macropores from fine to very fine, compaction-induced dewatering and strong permeability reduction. The base of the marl interval also shows increasing CEC and smectite content, resulting in a bound water content that rises with depth up to moderate values and that may be released at greater depths. In contrast, chalks show higher

permeability and low potential for fluid production with negligible bound water content and cemented macropores whose size rises with depth.

3. Units V and VI are mostly composed of mesoporous very low permeability calcite-cemented volcaniclastic materials with very high hydrous mineral (smectites, zeolites, and opal) content, associated with significant potential for bound water release as already suggested by the occurrence of several freshening anomalies. The top of Units V and VI likely hosts local zones of higher porosity and permeability due to the occurrence of additional macropores that may be alternative locations for the future décollement to form.

Data Availability Statement

This research used data provided by the International Ocean Discovery Program (IODP) and freely available on the LIMS Report Interface Page at http://web.iodp.tamu.edu/LORE or on the log database (http://mlp.ldeo.columbia.edu/logdb/scientific_ocean_drilling). Post-cruise data are available in the OTELo Research Data Repository (https://doi.org/10.24396/ORDAR-37 for petrophysical and geochemical data and https://doi.org/10.24396/ORDAR-39 for XRD data).

Acknowledgments

We greatly acknowledge the funding of the shore-based measurements of CNRS-INSU and IODP-France. We thank David Billet, Philippe Rousselle, Maximilien Beuret, Valérie Goncalves, Géraldine Kitzinger, and Hervé Marmier from the LIEC laboratory in Nancy and Metz (France) for running CEC, exchangeable cation composition, and soluble chloride content analyses. We also thank Angelina Razafitianamaharavo from the LIEC laboratory in Vandoeuvre-lès-Nancy, France, for performing nitrogen adsorption/desorption experiments. We finally acknowledge Danièle Bartier and Lise Salsi for their support in the XRD and calcimetry analyses. Finally, we would like to thank Pierre Henry and the second anonymous reviewer for their very constructive comments that greatly helped to improve the manuscript.

References

Archie, G. E. (1942). The electrical resistivity log as an aid in determining some reservoir characteristics. *Transactions of the American Institute of Mining, Metallurgical and Petroleum Engineers*, *146*, 54–62. https://doi.org/10.2118/942054-g

Bangs, N. L., Shipley, T. H., Moore, C., & Moore, G. F. (1999). Fluid accumulation and channeling along the northern Barbados Ridge décollement thrust. *Journal of Geophysical Research*, *104*(B9), 20,399–20,414. https://doi.org/10.1029/1999JB900133

Bangs, N. L. B., Shipley, T. H., Gulick, S. P. S., Moore, G. F., Kuromoto, S., & Nakamura, Y. (2004). Evolution of the Nankai Trough décollement from the trench into the seismogenic zone: Inferences from three-dimensional seismic reflection imaging. *Geology*, *32*(4), 273–276. https://doi.org/10.1130/G20211.2

Barnes, P. M., Lamarche, G., Bialas, J., Henrys, S., Pecher, I., Netzeband, G. L., et al. (2010). Tectonic and geological framework for gas hydrates and cold seeps on the Hikurangi subduction margin New Zealand. *Marine Geology*, *272*(1–4), 26–48. https://doi.org/10.1016/j.margeo.2009.03.012

Barnes, P. M., Wallace, L. M., Saffer, D. M., Bell, R. E., Underwood, M. B., Fagereng, A., et al. (2020). Slow slip source characterized by lithological and geometric heterogeneity. *Science Advances*, *6*(13), eaay3314. https://doi.org/10.1126/sciadv.aay3314

Barnes, P. M., Wallace, L. M., Saffer, D. M., Pecher, I. A., Petronotis, K. E., LeVay, L. J., et al. (2019). Site U1520. In L. M. Wallace, D. M. Saffer, P. M. Barnes, I. A. Pecher, K. E. Petronotis, L. J. LeVay, & The Expedition 372/375 Scientists (Eds.), *Hikurangi subduction margin coring, logging, and observatories*, *Proceedings of the International Ocean Discovery Program* (Vol. 372B/375). College Station, TX: International Ocean Discovery Program. https://doi.org/10.14379/iodp.proc.372B375.105.2019

Bartlow, N. M., Wallace, L. M., Beavan, R. J., Bannister, S., & Segall, P. (2014). Time-dependent modeling of slow slip events and associated seismicity and tremor at the Hikurangi subduction zone New Zealand. *Journal of Geophysical Research: Solid Earth*, *119*, 734–753. https://doi.org/10.1002/2013JB010609

Bassett, D., Sutherland, R., & Henrys, S. (2014). Slow wavespeeds and fluid overpressure in a region of shallow geodetic locking and slow slip Hikurangi subduction margin, New Zealand. *Earth and Planetary Science Letters*, *389*, 1–13. https://doi.org/10.1016/j.epsl.2013.12.021

Beavan, J., Wallace, L., Douglas, A., & Fletcher, H. (2007). Slow slip events on the Hikurangi subduction interface, New Zealand. In P. Tregoning & C. Rizos (Eds.), *Dynamic planet, monitoring and understanding a dynamic planet with geodetic and oceanographic tools* (pp. 438–444). Berlin: Springer.

Bekins, B. A., & Dreiss, S. J. (1992). A simplified analysis of parameters controlling dewatering in accretionary prisms. *Earth and Planetary Science Letters*, *109*(3–4), 275–287. https://doi.org/10.1016/0012-821x(92)90092-a

Bekins, B. A., McCaffrey, A. M., & Dreiss, J. D. (1995). Episodic and constant flow models for the origin of low-chloride waters in a modern accretionary complex. *Water Resources Research*, *31*(12), 3205–3215. https://doi.org/10.1029/95WR02569

Bell, R., Sutherland, R., Barker, D. H. N., Henrys, S., Bannister, S., Wallace, L., & Beavan, J. (2010). Seismic reflection character of the Hikurangi subduction interface, New Zealand, in the region of repeated Gisborne slow slip events. *Geophysical Journal International*, *180*(1), 34–48. https://doi.org/10.1111/j.1365-246X.2009.04401.x

Bilek, S. L., & Lay, T. (2002). Tsunami earthquakes possibly widespread manifestations of frictional conditional stability: Variability of Greenland accumulation. *Geophysical Research Letters*, *29*(14), 18-1–18-4. https://doi.org/10.1029/2002GL015215

Blum, P. (1997). Physical properties handbook: A guide to the shipboard measurement of physical properties of deep-sea cores (online), Tech. Note 26, Ocean Drill. Program, College Station, Tex. Retrieved from http://www-odp.tamu.edu/publications/tnotes/tn26/INDEX.HTM

Bourlange, S., & Henry, P. (2007). Numerical model of fluid pressure solitary wave propagation along the décollement of an accretionary wedge: Application to the Nankai wedge: Fluid pressure solitary wave propagation. *Geofluids*, *7*(3), 323–334. https://doi.org/10.1111/j.1468-8123.2007.00181.x

Bourlange, S., Henry, P., Moore, J. C., Mikada, H., & Klaus, A. (2003). Fracture porosity in the décollement zone of Nankai accretionary wedge using logging while drilling resistivity data. *Earth and Planetary Science Letters*, *209*(1–2), 103–112. https://doi.org/10.1016/S0012-821X(03)00082-7

Bray, C. J., & Karig, D. E. (1985). Porosity of sediments in accretionary prisms and some implications for dewatering processes. *Journal of Geophysical Research*, *90*(B1), 768–778. https://doi.org/10.1029/JB090iB01p00768

Brown, K. M., & Ransom, B. (1996). Porosity corrections for smectite-rich sediments: Impact on studies of compaction, fluid generation, and tectonic history. *Geology*, *24*(9), 843–846. http://doi.org/10.1130/0091-7613(1996)024%3c0843:PCFSRS%3e2.3.CO;2

Bussian, A. E. (1983). Electrical conductance in a porous medium. *Geophysics*, *48*(9), 1258–1268. https://doi.org/10.1190/1.1441549

Carr, H. Y., & Purcell, E. M. (1954). Effects of diffusion on free precession in nuclear magnetic resonance experiments. *Physical Review*, *94*(3), 630–638. https://doi.org/10.1103/PhysRev.94.630

Cheng, K., & Heidari, Z. (2017). Combined interpretation of NMR and TGA measurements to quantify the impact of relative humidity on hydration of clay minerals. *Applied Clay Science*, *143*, 362–371. https://doi.org/10.1016/j.clay.2017.04.006

Cochrane, G. R., Moore, J. C., MacKay, M. E., & Moore, G. F. (1994). Velocity and inferred porosity model of the Oregon accretionary prism from multichannel seismic data: Implications on sediment dewatering and overpressure. *Journal of Geophysical Research*, *99*(B4), 7033–7043. https://doi.org/10.1029/93JB03206

Conin, M., Henry, P., Bourlange, S., Raimbourg, H., & Reuschlé, T. (2011). Interpretation of porosity and LWD resistivity from the Nankai accretionary wedge in light of clay physicochemical properties: Evidence for erosion and local overpressuring: Porosity and LWD resistivity from Nankai. *Geochemistry, Geophysics, Geosystems*, *12*, Q0AD07. https://doi.org/10.1029/2010GC003381

Crutchley, G. J., Klaeschen, D., Henrys, S. A., Pecher, I. A., Mountjoy, J. J., & Woelz, S. (2020). Subducted sediments, upper-plate deformation and dewatering at New Zealand's southern Hikurangi subduction margin. *Earth and Planetary Science Letters*, *530*, 115945. https://doi.org/10.1016/j.epsl.2019.115945

Daigle, H. (2014). Microporosity development in shallow marine sediments from the Nankai Trough. *Marine Geology*, *357*, 293–303. https://doi.org/10.1016/j.margeo.2014.09.041

Daigle, H., Thomas, B., Rowe, H., & Nieto, M. (2014). Nuclear magnetic resonance characterization of shallow marine sediments from the Nankai Trough, Integrated Ocean Drilling Program Expedition 333: NMR of Nankai Trough sediments. *Journal of Geophysical Research: Solid Earth*, *119*, 2631–2650. https://doi.org/10.1002/2013JB010784

Davy, B., Hoernle, K., & Werner, R. (2008). Hikurangi Plateau: Crustal structure, rifted formation, and Gondwana subduction history: Hikurangi plateau-crustal structure and history. *Geochemistry, Geophysics, Geosystems*, *9*, Q07004. https://doi.org/10.1029/2007GC001855

De Boer, J. H. (1958). The structure and properties of porous materials. In *Proceedings of the Tenth Symposium of the Colston Research Society Held in the University of Bristol* (pp. 68–94). London: Butterworths.

Dean, S. M., McNeill, L. C., Henstock, T. J., Bull, J. M., Gulick, S. P. S., Austin, J. A., et al. (2010). Contrasting décollement and prism properties over the Sumatra 2004–2005 earthquake rupture boundary. *Science*, *329*(5988), 207–210. https://doi.org/10.1126/science.1189373

Dennis, B. (1997). *Pores explored. Middle East well evaluation review* (Vol. 19, pp. 53–65). Schlumberger.

Derkowski, A., Środoń, J., & McCarty, D. K. (2015). Cation exchange capacity and water content of opal in sedimentary basins: Example from the Monterey Formation, California. *American Mineralogist*, *100*(5–6), 1244–1256. https://doi.org/10.2138/am-2015-5008

Doser, D. I., & Webb, T. H. (2003). Source parameters of large historical (1917–1961) earthquakes, North Island, New Zealand. *Geophysical Journal International*, *152*(3), 795–832. https://doi.org/10.1046/j.1365-246X.2003.01895.x

Dunn, K. J., Bergman, D. J., & LaTorraca, G. A. (2002). *Nuclear magnetic resonance: Petrophysical and logging applications, handbook of geophysical exploration: Seismic exploration* (Vol. 32, pp. 1–293). Kidlington, Oxford, UK: Pargamon.

Dutilleul, J., Bourlange, S., Conin, M., & Géraud, Y. (2020). Quantification of bound water content, interstitial porosity and fracture porosity in the sediments entering the North Sumatra subduction zone from cation exchange capacity and IODP Expedition 362 resistivity data. *Marine and Petroleum Geology*, *111*, 156–165. https://doi.org/10.1016/j.marpetgeo.2019.08.007

Ellis, D. V., & Singer, J. M. (2007). *Well logging for Earth scientists*. Dordrecht, The Netherlands: Springer. https://doi.org/10.1007/978-1-4020-4602-5

Ellis, S., Fagereng, Å., Barker, D., Henrys, S., Saffer, D., Wallace, L., et al. (2015). Fluid budgets along the northern Hikurangi subduction margin, New Zealand: The effect of a subducting seamount on fluid pressure. *Geophysical Journal International*, *202*(1), 277–297. https://doi.org/10.1093/gji/ggv127

Fagereng, Å., Diener, J. F. A., Ellis, S., & Remitti, F. (2018). Fluid-related deformation processes at the up- and downdip limits of the subduction thrust seismogenic zone: What do the rocks tell us? In T. Byrne et al. (Eds.), *Geology and tectonics of subduction zones: A tribute to Gaku Kimura: Geological Society of America Special Paper* (Vol. 534, pp. 187–215). Boulder, Colorado, USA: The Geological Society of America. https://doi.org/10.1130/2018.2534(12)

Fagereng, Å., Savage, H. M., Morgan, J. K., Wang, M., Meneghini, F., Barnes, P. M., et al. (2019). Mixed deformation styles observed on a shallow subduction thrust Hikurangi margin, New Zealand. *Geology*, *47*(9), 872–876. https://doi.org/10.1130/G46367.1

Ferrage, E. (2016). Investigation of the interlayer organization of water and ions in smectite from the combined use of diffraction experiments and molecular simulations. A review of methodology, applications and perspectives. *Clays and Clay Minerals*, *64*(4), 348–373. https://doi.org/10.1346/CCMN.2016.0640401

Ferrage, E., Lanson, B., Sakharov, B. A., & Drits, V. A. (2006). Investigation of smectite hydration properties by modeling experimental X-ray diffraction patterns: Part I. Montmorillonite hydration properties. *American Mineralogist*, *90*(8–9), 1358–1374. https://doi.org/10.2138/am.2005.1776

Fitts, T. G., & Brown, K. M. (1999). Stress-induced smectite dehydration: Ramifications for patterns of freshening and fluid expulsion in the N. Barbados accretionary wedge. *Earth and Planetary Science Letters*, *172*(1–2), 179–197. https://doi.org/10.1016/S0012-821X(99)00168-5

Geersen, J., McNeill, L., Henstock, T. J., & Gaedicke, C. (2013). The 2004 Aceh-Andaman earthquake: Early clay dehydration controls shallow seismic rupture: Shallow rupture off northern Sumatra. *Geochemistry, Geophysics, Geosystems*, *14*, 3315–3323. https://doi.org/10.1002/ggge.20193

Grunewald, E., & Knight, R. (2009). A laboratory study of NMR relaxation times and pore coupling in heterogeneous media. *Geophysics*, *74*, E215eE221. https://doi.org/10.1190/1.3223712

Henry, P. (1997). Relationship between porosity, electrical conductivity and cation exchange capacity in Barbados wedge sediments. In *Proceedings of the Ocean Drilling Program Scientific Results* (Vol. 156, pp. 137–149). College Station, TX: Ocean Drilling Program. https://doi.org/10.2973/odp.proc.sr.156.020.1997

Henry, P., & Bourlange, S. (2004). Smectite and fluid budget at Nankai IODP sites derived from cation exchange capacity. *Earth and Planetary Science Letters*, *219*(1–2), 129–145. https://doi.org/10.1016/S0012-821X(03)00694-0

Holtzapffel, T. (1985). Les minéraux argileux, Préparation. In *Analyse diffractométrique et détermination* (Vol. 12, pp. 3–136). Villeneuve d'Ascq, France: Société Géologique du Nord.

Hüpers, A., & Kopf, A. J. (2012). Effect of smectite dehydration on pore water geochemistry in the shallow subduction zone: An experimental approach. *Geochemistry, Geophysics, Geosystems*, *13*, Q0AD26. https://doi.org/10.1029/2012GC004212

Hüpers, A., Torres, M. E., Owari, S., McNeill, L. C., Dugan, B., Henstock, T. J., et al. (2017). Release of mineral-bound water prior to subduction tied to shallow seismogenic slip off Sumatra. *Science*, *356*(6340), 841–844. https://doi.org/10.1126/science.aal3429

Janssen, C., Wirth, R., Reinicke, A., Rybacki, E., Naumann, R., Wenk, H.-R., & Dresen, G. (2011). Nanoscale porosity in SAFOD core samples (San Andreas Fault). *Earth and Planetary Science Letters*, *301*(1–2), 179–189. https://doi.org/10.1016/j.epsl.2010.10.040

Kameda, J., Hina, S., Kobayashi, K., Yamaguchi, A., Hamada, Y., Yamamoto, Y., et al. (2012). Silica diagenesis and its effect on interplate seismicity in cold subduction zones. *Earth and Planetary Science Letters*, *317–318*, 136–144. https://doi.org/10.1016/j.epsl.2011.11.041

Kastner, M., Solomon, E. A., Harris, R. N., & Torres, M. E. (2014). Fluid origins, thermal regimes, and fluid and solute fluxes in the forearc of subduction zones. In *Developments in marine geology* (Vol. 7, pp. 671–733). Amsterdam, Netherlands: Elsevier. https://doi.org/10.1016/B978-0-444-62617-2.00022-0

Katz, A. J., & Thompson, A. H. (1986). Quantitative prediction of permeability in porous rock. *Physical Review B*, *34*(11), 8179–8181. https://doi.org/10.1103/PhysRevB.34.8179

Katz, A. J., & Thompson, A. H. (1987). Prediction of rock electrical conductivity from mercury injection measurements. *Journal of Geophysical Research*, *92*(B1), 599–607. https://doi.org/10.1029/JB092iB01p00599

Kitajima, H., & Saffer, D. M. (2014). Consolidation state of incoming sediments to the Nankai Trough subduction zone: Implications for sediment deformation and properties. *Geochemistry, Geophysics, Geosystems*, *15*, 2821–2839. https://doi.org/10.1002/2014GC005360

Kodaira, S., Iidaka, T., Kato, A., Park, J.-O., Iwasaki, T., & Kaneda, Y. (2004). High pore fluid pressure may cause silent slip in the Nankai Trough. *Science*, *304*(5675), 1295–1298. https://doi.org/10.1126/science.1096535

Koulali, A., McClusky, S., Wallace, L., Allgeyer, S., Tregoning, P., D'Anastasio, E., & Benavente, R. (2017). Slow slip events and the 2016 Te Araroa M_w 7.1 earthquake interaction: Northern Hikurangi subduction, New Zealand: Slow slip and the Te Araroa earthquake. *Geophysical Research Letters*, *44*, 8336–8344. https://doi.org/10.1002/2017GL074776

Labani, M. M., Rezaee, R., Saeedi, A., & Hinai, A. A. (2013). Evaluation of pore size spectrum of gas shale reservoirs using low pressure nitrogen adsorption, gas expansion and mercury porosimetry: A case study from the Perth and Canning Basins, Western Australia. *Journal of Petroleum Science and Engineering*, *112*, 7–16. https://doi.org/10.1016/j.petrol.2013.11.022

Lai, J., & Wang, G. (2015). Fractal analysis of tight gas sandstones using high-pressure mercury intrusion techniques. *Journal of Natural Gas Science and Engineering*, *24*, 185–196. https://doi.org/10.1016/j.jngse.2015.03.027

Li, Y., & Wardlaw, N. C. (1986). The influence of wettability and critical pore-throat size ratio on snap-off. *Journal of Colloid and Interface Science*, *109*(2), 461–472. https://doi.org/10.1016/0021-9797(86)90324-3

Liu, Y., & Rice, J. R. (2007). Spontaneous and triggered aseismic deformation transients in a subduction fault model. *Journal of Geophysical Research*, *112*, B09404. https://doi.org/10.1029/2007JB004930

Marschall, D., Gardner, J. S., Mardon, D., & Coates, R. (1995). Method for correlating NMR relaxometry and mercury injection data. Presented at the Society of Core Analysts International Symposium, San Francisco, California, USA, 12–14 September. SCA-9511.

Meiboom, S., & Gill, D. (1958). Modified spin-echo method for measuring nuclear relaxation times. *Review of Scientific Instruments*, *29*(7), 662–691. https://doi.org/10.1063/1.1716293

Mikada, H., Moore, G.F., Taira, A., Becker, K., Moore, J. C., & Klaus, A. (Eds.) (2005). *Proceedings of the Ocean Drilling Program, Scientific Results, 190/196* (pp. 1–26). College Station, TX: Ocean Drilling Program. https://doi.org/10.2973/odp.proc.sr.190196.201.2005

Moore, G. F., & Shipley, T. H. (1993). Character of the décollement in the Leg 131 area, Nankai Through. In Hill, I. A. et al. (Eds.), *Proceedings of the Ocean Drilling Program Scientific Results* (Vol. *131*, pp. 73–82). College Station, TX: Ocean Drilling Program. https://doi.org/10.2973/odp.proc.sr.131.111.1993

Moore, J. C., Klaus, A., Bangs, N. L., Bekins, B., Bücker, C. J., Brückmann, W., et al. (1998). Consolidation patterns during initiation and evolution of a plate-boundary decollement zone: Northern Barbados accretionary prism. *Geology*, *26*(9), 811–814. https://doi.org/10.1130/0091-7613(1998)026%3c0811:cpdiae%3e2.3.co;2

Moore, J. C., & Vrolijk, P. (1992). Fluids in accretionary prisms. *Reviews of Geophysics*, *30*(2), 113–135. https://doi.org/10.1029/92RG00201

Nishiyama, N., & Yokoyama, T. (2014). Estimation of permeability of sedimentary rocks by applying water-expulsion porosimetry to Katz and Thompson model. *Engineering Geology*, *177*, 75–82. https://doi.org/10.1016/j.enggeo.2014.05.016

Nooruddin, H. A., Hossain, M. E., Al-Yousef, H., & Okasha, T. (2014). Comparison of permeability models using mercury injection capillary pressure data on carbonate rock samples. *Journal of Petroleum Science and Engineering*, *121*, 9–22. https://doi.org/10.1016/j.petrol.2014.06.032

Obara, K. (2002). Nonvolcanic deep tremor associated with Subduction in Southwest Japan. *Science*, *296*(5573), 1679–1681. https://doi.org/10.1126/science.1070378

Pabalan, R. T., & Bertetti, F. P. (2001). Cation-exchange properties of natural zeolites. *Reviews in Mineralogy and Geochemistry*, *45*(1), 453–518. https://doi.org/10.2138/rmg.2001.45.14

Plaza-Faverola, A., Henrys, S., Pecher, I., Wallace, L., & Klaeschen, D. (2016). Splay fault branching from the Hikurangi subduction shear zone: Implications for slow slip and fluid flow: PSDM seismic across the Hikurangi margin. *Geochemistry, Geophysics, Geosystems*, *17*, 5009–5023. https://doi.org/10.1002/2016GC006563

Plaza-Faverola, A., Klaeschen, D., Barnes, P., Pecher, I., Henrys, S., & Mountjoy, J. (2012). Evolution of fluid expulsion and concentrated hydrate zones across the southern Hikurangi subduction margin, New Zealand: An analysis from depth migrated seismic data: Hikurangi hydrate zones from PSDM. *Geochemistry, Geophysics, Geosystems*, *13*, Q08018. https://doi.org/10.1029/2012GC004228

Pytte, A. M., & Reynolds, R. C. (1989). The thermal transformation of smectite to illite. In N. D. Naeser & T. H. McCulloh (Eds.), *Thermal history of sedimentary basins* (pp. 133–140). New York: Springer. https://doi.org/10.1007/978-1-4612-3492-0_8

Ransom, B., & Helgeson, H. C. (1995). A chemical and thermodynamic model of dioctahedral 2 layer clay minerals in diagenetic processes; dehydration of smectite as a function of temperature and depth in sedimentary basins. *American Journal of Science*, *295*(3), 245–281. https://doi.org/10.2475/ajs.295.3.245

Reeves, G. M., Sims, I., Cripps, J. C., & London, G. S. (2006). *Clay materials used in construction* (Vol. 21). London, UK: Geological Society Special Publications, Engineering Geology Special Publication.

Revil, A. (2002). Electrical properties of zeolitized volcaniclastic materials. *Journal of Geophysical Research*, *107*(B8), 107. https://doi.org/10.1029/2001JB000599

Revil, A., Cathles, L. M. III, Losh, S., & Nunn, J. A. (1998). Electrical conductivity in shaly sands with geophysical applications. *Journal of Geophysical Research*, *103*(B10), 23,925–23,936. https://doi.org/10.1029/98JB02125

Rosenbrand, E., Fabricius, I. L., Fisher, Q., & Grattoni, C. (2015). Permeability in Rotliegend gas sandstones to gas and brine as predicted from NMR, mercury injection and image analysis. *Marine and Petroleum Geology*, *64*, 189–202. https://doi.org/10.1016/j.marpetgeo.2015.02.009

Rosener, M., & Géraud, Y. (2007). Using physical properties to understand the porosity network geometry evolution in gradually altered granites in damage zones. *Geological Society, London, Special Publications*, *284*(1), 175–184. https://doi.org/10.1144/SP284.12

Saffer, D. M. (2003). Pore pressure development and progressive dewatering in underthrust sediments at the Costa Rican subduction margin: Comparison with northern Barbados and Nankai. *Journal of Geophysical Research*, *108*(B5), 2261. https://doi.org/10.1029/2002JB001787

Saffer, D. M., & Tobin, H. J. (2011). Hydrogeology and mechanics of subduction zone forearcs: Fluid flow and pore pressure. *Annual Review of Earth and Planetary Sciences*, *39*(1), 157–186. https://doi.org/10.1146/annurev-earth-040610-133408

Saffer, D. M., & Wallace, L. M. (2015). The frictional, hydrologic, metamorphic and thermal habitat of shallow slow earthquakes. *Nature Geoscience*, *8*(8), 594–600. https://doi.org/10.1038/ngeo2490

Saffer, D. M., Wallace, L. M., Barnes, P. M., Pecher, I. A., Petronotis, K. E., LeVay, L. J., et al. (2019). Expedition 372B/375 summary. In Wallace, L. M., Saffer, D. M., Barnes, P. M., Pecher, I. A., Petronotis, K. E., LeVay, L. J., and The Expedition 372/375 Scientists, Hikurangi Subduction Margin Coring, Logging, and Observatories. Proceedings of the International Ocean Discovery Program, 372B/375: College Station, TX (International Ocean Discovery Program). https://doi.org/10.14379/iodp.proc.372B375.101.2019

Schmitt, M., Fernandes, C. P., da Cunha Neto, J. A. B., Wolf, F. G., & dos Santos, V. S. S. (2013). Characterization of pore systems in seal rocks using nitrogen gas adsorption combined with mercury injection capillary pressure techniques. *Marine and Petroleum Geology*, *39*(1), 138–149. https://doi.org/10.1016/j.marpetgeo.2012.09.001

Screaton, E., Saffer, D., Henry, P., & Hunze, S. (2002). Porosity loss within the underthrust sediments of the Nankai accretionary complex: Implications for overpressures. *Geology*, *30*(1), 19–22. https://doi.org/10.1130/0091-7613(2002)030%3c0019:PLWTUS%3e2.0.CO;2

Seno, T. (2002). Tsunami earthquakes as transient phenomena. *Geophysical Research Letters*, *29*(10), 58-1–58-4. https://doi.org/10.1029/2002GL014868

Shaddox, H. R., & Schwartz, S. Y. (2019). Subducted seamount diverts shallow slow slip to the forearc of the northern Hikurangi subduction zone New Zealand. *Geology*, *47*(5), 415–418. https://doi.org/10.1130/G45810.1

Shipley, T. H., Moore, G. F., Bangs, N., Moore, J. C., & Stoffa, P. L. (1994). Seismically inferred dilatancy distribution, northern Barbados Ridge decollement: Implications for fluid migration and fault strength. *Geology*, *22*(5), 411–414. https://doi.org/10.1130/0091-7613(1994)022%3c0411:SIDDNB%3e2.3.CO;2

Sing, K. S., Everett, D. H., Haul, R. A. W., Moscou, L., Pierotti, R. A., Rouquerol, J., & Siemieniewsha, T. (1985). Reporting physisorption data for gas/solid systems with special reference to the determination of surface area and porosity. *Pure and Applied Chemistry*, *57*(4), 603–619. https://doi.org/10.1351/pac198557040603

Soueid Ahmed, A., Revil, A., Byrdina, S., Coperey, A., Gailler, L., Grobbe, N., et al. (2018). 3D electrical conductivity tomography of volcanoes. *Journal of Volcanology and Geothermal Research*, *356*, 243–263. https://doi.org/10.1016/j.jvolgeores.2018.03.017

Spinelli, G. A., Saffer, D. M., & Underwood, M. B. (2006). Hydrogeologic responses to three-dimensional temperature variability Costa Rica subduction margin. *Journal of Geophysical Research*, *111*, B04403. https://doi.org/10.1029/2004JB003436

Tessier, A., Campbell, P. G. C., & Bisson, M. (1979). Sequential extraction procedure for the speciation of particulate trace metals. *Analytical Chemistry*, *51*(7), 844–851. https://doi.org/10.1021/ac50043a017

Thiry, M., Carrillo, N., Franke, C., & Martineau, N. (2013). Technique de préparation des minéraux argileux en vue de l'analyse par diffraction des Rayons X et introduction à l'interprétation des diagrammes. In *Rapport technique n° RT131010MTHI* (pp. 1–34). Fontainebleau, France: Ecole des Mines de Paris. https://hal.archives-ouvertes.fr/hal-00872214/

Todd, E. K., Schwartz, S. Y., Mochizuki, K., Wallace, L. M., Sheehan, A. F., Webb, S. C., et al. (2018). Earthquakes and tremor linked to seamount subduction during shallow slow slip at the Hikurangi margin New Zealand. *Journal of Geophysical Research: Solid Earth*, *123*, 6769–6783. https://doi.org/10.1029/2018JB016136

Underwood, M. B. (2007). Sediment inputs to subduction zones: Why lithostratigraphy and clay mineralogy matter. In T. H. Dixon & C. Moore (Eds.), *The seismogenic zone of subduction thrust faults*. New York Chichester, West Sussex: Columbia University Press.

Vincent, B., Fleury, M., Santerre, Y., Brigaud, B. (2011). NMR relaxation of neritic carbonates: An integrated petrophysical and petrographical approach. *Journal of Applied Geophysics*, *74*(1), 38–58. https://doi.org/10.1016/j.jappgeo.2011.03.002

Wallace, L. M. (2020). Slow Slip Events in New Zealand. *Annual Review of Earth and Planetary Sciences*, *48*(1), 175–203. https://doi.org/10.1146/annurev-earth-071719-055104

Wallace, L. M., & Beavan, J. (2010). Diverse slow slip behavior at the Hikurangi subduction margin New Zealand. *Journal of Geophysical Research*, *115*, B12402. https://doi.org/10.1029/2010JB007717

Wallace, L. M., Beavan, J., Bannister, S., & Williams, C. (2012). Simultaneous long-term and short-term slow slip events at the Hikurangi subduction margin, New Zealand: Implications for processes that control slow slip event occurrence, duration, and migration. *Journal of Geophysical Research*, *117*, B11402. https://doi.org/10.1029/2012JB009489

Wallace, L. M., Beavan, J., McCaffrey, R., & Desmond, D. (2004). Subduction zone coupling and tectonic block rotations in the North Island, New Zealand. *Journal of Geophysical Research*, *109*, B12406. https://doi.org/10.1029/2004JB003241

Wallace, L. M., Kaneko, Y., Hreinsdóttir, S., Hamling, I., Peng, Z., Bartlow, N., et al. (2017). Large-scale dynamic triggering of shallow slow slip enhanced by overlying sedimentary wedge. *Nature Geoscience*, *10*, 765–770. https://doi.org/10.1038/ngeo3021

Wallace, L. M., Saffer, D. M., Barnes, P. M., Pecher, I. A., Petronotis, K. E., LeVay, L. J., et al. (2019). Expedition 372B/375 methods. In Wallace, L. M., Saffer, D. M., Barnes, P. M., Pecher, I. A., Petronotis, K. E., LeVay, L. J., and The Expedition 372/375 Scientists (Eds.), *Hikurangi Subduction Margin Coring, Logging, and Observatories, Proceedings of the International Ocean Discovery Program* (Vol. *372B/375*. College Station, TX: International Ocean Discovery Program. https://doi.org/10.14379/iodp.proc.372B375.105.2019

Wallace, L. M., Webb, S. C., Ito, Y., Mochizuki, K., Hino, R., Henrys, S., et al. (2016). Slow slip near the trench at the Hikurangi subduction zone New Zealand. *Science*, *352*, 701–704. https://doi.org/10.1126/science.aaf2349

Yuan, Y., Rezaee, R., Verrall, M., Hu, S.-Y., Zou, J., & Testmanti, N. (2018). Pore characterization and clay bound water assessment in shale with a combination of NMR and low-pressure nitrogen gas adsorption. *International Journal of Coal Geology*, *194*, 11–21. https://doi.org/10.1016/j.coal.2018.05.003

Zhao, H., Ning, Z., Wang, Q., Zhang, R., Zhao, T., Niu, T., & Zeng, Y. (2015). Petrophysical characterization of tight oil reservoirs using pressure-controlled porosimetry combined with rate-controlled porosimetry. *Fuel*, *154*, 233–242. https://doi.org/10.1016/j.fuel.2015.03.085